Journal of Sustainable Metallurgy
https://doi.org/10.1007/s40831-026-01488-x

THEMATIC SECTION: 9TH INTERNATIONAL SLAG VALORISATION SYMPOSIUM

Large-Scale Feasibility of the EnAM-Concept Demonstrated in the Pyrometallurgical Treatment of NMC Lithium-Ion Battery Black Mass and Full Cells

Hugo Lucas[1] · Fabian Diaz[2] · Cindytami Rachmawati[3] · Marko Ranneberg[4] · Joao Weiss[1] · Wei Song[1] · Robert Möckel[5] · Torsten Graupner[4] · Urs Peuker[3] · Bernd Friedrich[1]

Received: 15 October 2025 / Accepted: 16 March 2026

Abstract

Pyrometallurgical recycling of spent lithium-ion batteries enables efficient recovery of cobalt, nickel and copper, while lithium predominantly reports to the slag phase. Valorizing lithium-rich slags remains a key challenge, with limited pilot-scale data available on mass flows, energy demand and emissions. This study presents pilot-scale trials in a 300 L Top Blown Rotary Converter (TBRC), treating black mass and full end-of-life NMC cells under near-industrial conditions. Continuous monitoring and centralized data acquisition enabled complete mass and energy balances, time-resolved off-gas analysis and product characterization. A novel approach—Engineering of Artificial Minerals (EnAM)—was introduced, employing controlled cooling to promote γ-$LiAlO_2$ formation in slags, facilitating flotation-based lithium recovery. Key results include ~99% reduction efficiency for Cu, Ni and Co, and ~45% Mn transfer to metal for black mass feed. Energy consumption averaged ~8.5 kWh/kg, with approximately 62% supplied by the burner. Black mass treatments yielded higher HF emissions than full-cell treatments, while Al foils in full cells enhanced Mn partitioning into the slag–metal system. Controlled cooling at 25 °C/h, either directly after treatment (full battery cells) or after post-remelting (black mass), is beneficial for immobilizing lithium as γ-$LiAlO_2$. The EnAM from full battery cells immobilized 76% of the lithium present in the slag as γ-$LiAlO_2$, compared with 44% immobilized in the EnAM from black mass. These pilot-scale trials provide a dataset to support future life-cycle assessments and demonstrate that EnAM could be a viable pathway for lithium recovery when integrated with established pyrometallurgical practices.

The contributing editor for this article was U. Pal.

✉ Hugo Lucas
hlucas@ime-aachen.de

[1] IME Process Metallurgy and Metal Recycling, RWTH Aachen University, 52072 Aachen, Germany

[2] SMS Group GmbH, Am SMS Campus 1, 41069 Mönchengladbach, Germany

[3] Institute of Mechanical Process Engineering and Mineral Processing, TU Bergakademie Freiberg, 09599 Freiberg, Germany

[4] Federal Institute for Geosciences and Natural Resources (BGR), Stilleweg 2, 30655 Hannover, Germany

[5] Helmholtz-Zentrum Dresden-Rossendorf, Helmholtz Institute Freiberg for Resource Technology, Chemnitzer Straße 40, 09599 Freiberg, Germany

Published online: 10 April 2026

Graphical Abstract

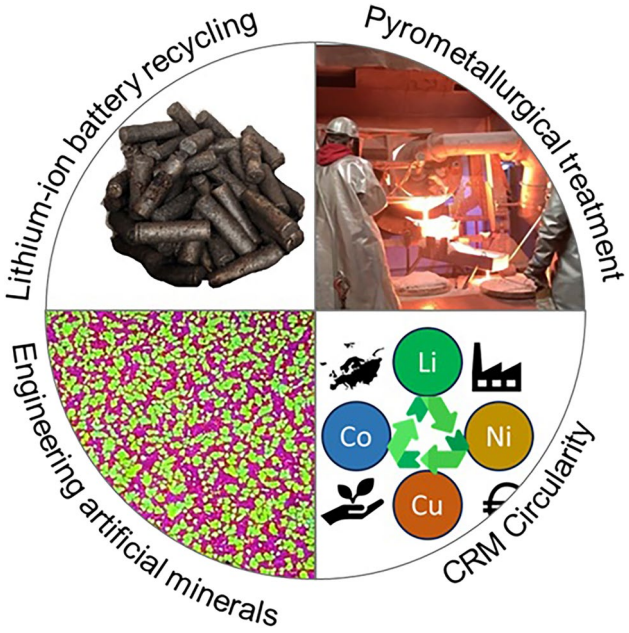

Keywords Pyrometallurgy · NMC lithium-ion batteries · LIB recycling · Slag engineering · EnAM

Introduction

Recycling lithium-ion batteries (LIBs) typically involves the mechanical separation of metals and graphite, thermolysis to break down organic materials, and either pyrometallurgical or hydrometallurgical steps [1–3]. Among these, pyrometallurgy is particularly robust for concentrating transition metals into alloys while directing lithium to either the slag or gas phase [4, 5].

Traditional processes, such as the Umicore method, primarily focus on reducing metals such as copper (Cu), cobalt (Co) and nickel (Ni) to form alloys while retaining manganese (Mn) and lithium in the slag [6, 7]. Slag formers—such as CaO, Al_2O_3 and SiO_2 are employed to control melting point and viscosity during the smelting process [6, 7]. Patent data define slag windows, e.g., 10–40% MnO with CaO–Li_2O/Al_2O_3 constraints or 25–70% MnO with limits on Al_2O_3, SiO_2 and Li_2O [8–10]. These compositional rules demonstrate deliberate stabilization of lithium in the slag while directing Ni and Co to metallic phases, thereby using the slag both as a lithium collector and as a medium for controlling metal–slag equilibria. In contrast, other patents outline volatilization pathways in which lithium is transferred into the off-gas during smelting, enabling its concentration in fumes for downstream recovery and usage of halogens as fuming agents [11–16]. Together, these examples illustrate the two principal lithium-management strategies in pyrometallurgy: retention in slags through compositional control or intentional volatilization into off-gases. Two studies provide explicit results, reporting lab-scale mass balances and high recovery efficiencies [13, 14]. Most other publications offer only conceptual insights on slag chemistry, lithium losses, or volatilization [15, 16], with no industrial energy, mass, or emissions datasets available. Despite detailed information on slag chemistry and process pathways at both industrial and academic levels, complete energy and mass balances at the plant scale, residence times and CO_2 emission inventories remain absent. Thus, while the patents clearly document mature pyrometallurgical technologies for NMC (nickel–manganese–cobalt oxide) battery recycling, they simultaneously highlight the proprietary nature of the critical datasets required for transparent life-cycle and techno-economic assessments.

Investigating hydrometallurgical approaches, some authors have demonstrated that nearly 100% lithium leaching efficiency can be achieved at 80 °C from lithium slag containing $LiAlSiO_4$ and Li_2SiO_3 phases [4]. However, direct leaching produces silica gel, which complicates filtration and subsequent extraction [17, 18]. Lithium recovery after pyrometallurgical treatment becomes difficult when the slag is in a silica-rich or amorphous structure.

As an alternative to traditional hydrometallurgy, the Engineered Artificial Minerals (EnAM) approach utilizes a pyrometallurgical process where the slag composition, cooling

conditions and crystallization are carefully controlled to induce the formation of specific mineral phases that contain the key element to be separated. In this case, lithium needs to be segregated into a mineral phase and a concentration that can be easily separated from the rest of the mineral bulk using methods such as mechanical enrichment and flotation [19]. For LIB treatment, a suitable EnAM would be the selective precipitation and immobilization of lithium in the γ-$LiAlO_2$ mineral phase, since it can be efficiently separated from the bulk by flotation [20].

The German Project LiBRi was the first to demonstrate that lithium aluminates (γ-$LiAlO_2$) generated in the slag mineralogy during the treatment of lithium cobalt oxide (LCO) batteries can be recovered by flotation [21]. Nevertheless, soon after, when similar trials were carried out on the NMC LIB family under similar conditions, slags showed no lithium–aluminum precipitates. To explain this behavior, the German GreenBatt Cluster created the Pyrolith project [22].

The Pyrolith project conducted an in-depth study of the Al_2O_3–SiO_2–CaO–Mn_xO_y–Li_2O mineral system to immobilize lithium in slag and to maximize the formation of lithium aluminates. Among the most important aspects of this project are the investigations by Ranneberg et al. on the characterization of slags rich in manganese and lithium oxides, which use UV light to highlight the different luminescence colors of the slag phases, allowing γ-$LiAlO_2$ (green in Fig. 1) to be easily and quickly identified [23–25].

Fig. 1 Photo of artificial Al_2O_3–SiO_2–CaO–MnO–Li_2O-type lithium-ion batteries (LIB) slags under short-wave UV radiation (254 nm). Because Mn-doped γ-$LiAlO_2$ appears green under short-wave UV light, this method is suitable for assessing the relative content, spatial distribution, grain size and grain shape of the target phase [26]. Sample size 2×5 cm

Figure 2a, b present analyses of experimental plans using artificial slags (simulants), similar to those depicted in Fig. 1, with varying lithium and manganese contents. These experiments demonstrated that the presence of manganese does not directly affect the crystallization of lithium aluminates (Fig. 2b) but promotes an increase in the amorphous phases (Fig. 2a). Therefore, low cooling rates are needed to minimize the influence of manganese, thereby increasing the crystalline character of the slag (EnAM). Maximizing the content of γ-$LiAlO_2$ is critical for recovering lithium from flotation treatments. According to Qiu et al. (2025), it is also possible to recover lithium from other mineral phases present in the slags, such as eucryptite (β-$LiAlSiO_4$), but more complex floating and leaching steps are necessary [27].

Engineering of artificial minerals (EnAM) overcomes these difficulties through controlled segregation and strategic crystallization, producing mineral phases that can be separated by other means [29, 30]. This is the case of LIBs, where the aim is to maximize the formation of γ-$LiAlO_2$ for subsequent separation via flotation [17]. The use of advanced thermochemical software, such as FactSage, to model the mineral phases that can precipitate in lithium- and manganese-rich slags proved unreliable, requiring in-depth research, including variations in compositions, to create γ-$LiAlO_2$ and improve the existing thermodynamic database and design diagrams, such as those shown in Fig. 3 [28, 31].

EnAM, on a large scale, requires one unit to treat LIB material and another to ensure low-control cooling of the produced slag.

Pyrometallurgical processing is widely used for recycling spent lithium-ion batteries to recover transition metals, such as Co, Ni, and Cu, while lithium is mostly retained in the slag. Yet, the valorization of these slags remains underexplored, and very few studies address how lithium can be

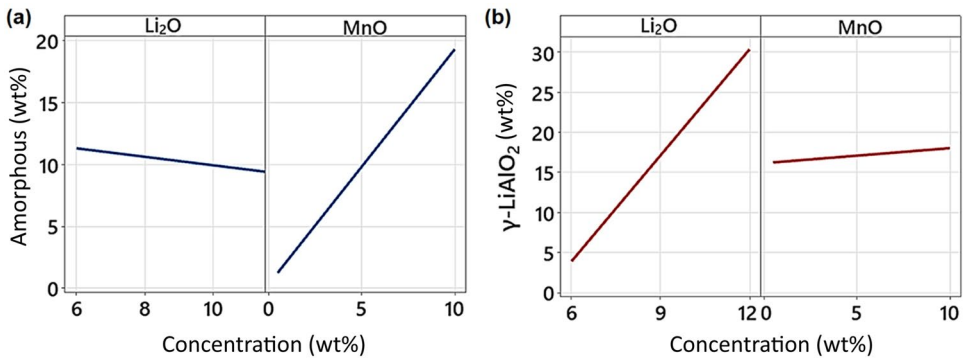

Fig. 2 Plan of experiments with artificial LIBs slags of Al_2O_3–SiO_2–CaO varying the MnO and Li_2O content with cooling rates of 25 °C/h; **a** amorphous content and **b** γ-$LiAlO_2$ content [25, 28]

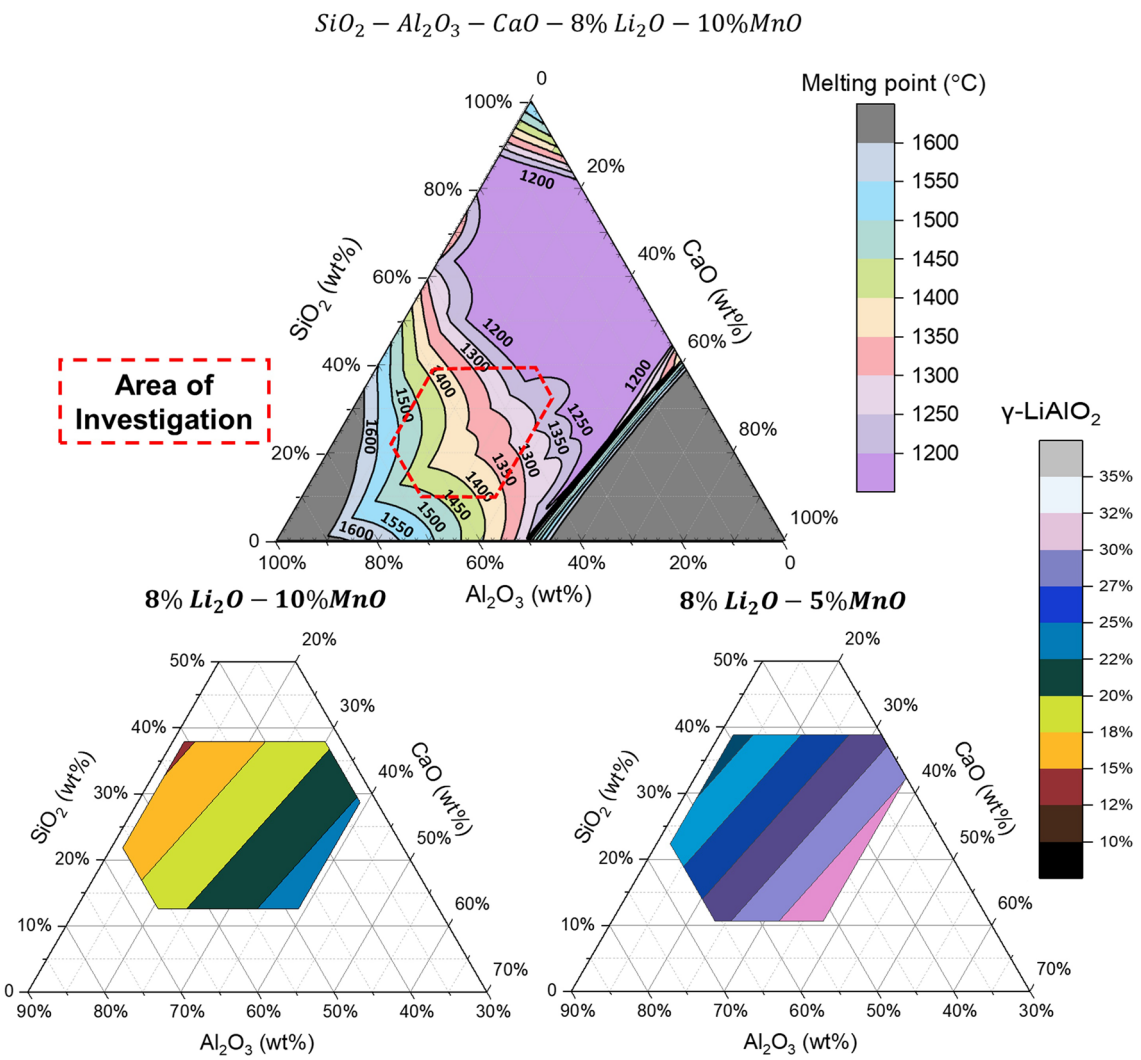

Fig. 3 Optimization of SiO_2–Al_2O_3–CaO–(8% Li_2O–5% MnO) and (8% Li_2O–10% MnO) mineral matrix to promote the precipitation of γ-$LiAlO_2$ under low cooling conditions (25 °C/h) [28]

effectively stabilized and recovered. Despite the continued industrial use of pyrometallurgical routes, realistic datasets on mass flows, energy consumption and emissions are rarely disclosed, forcing assessments to rely on laboratory-scale approximations.

This work addresses this gap by treating black mass and full NMC cells in a pilot-scale top-blown rotary converter (TBRC) equipped with sensors and a centralized data acquisition system to monitor process variables, energy flows and gas emissions throughout operation. The strategy builds on pyrometallurgical robustness for multi-waste feedstocks, while enabling lithium recovery through EnAM. Controlled cooling promotes the crystallization of lithium aluminates ($LiAlO_2$), which can be separated by flotation [17]. The proposed process was benchmarked against a pure pyrometallurgical treatment of black mass, which had a minimized iron concentration owing to casing removal but similar process conditions, serving as a reference case. The objective is to provide transparent mass and energy balances, emissions data and slag mineralogy under near-industrial conditions of the EnAM, thereby supporting realistic comparisons of different pyrometallurgical strategies and enabling integration into life-cycle and techno-economic assessments.

Methodology

For the pilot-scale experiments, pyrolyzed lithium battery materials from the NMC family were used, processed by ACCUREC Recycling GmbH. This study presents two pilot-scale tests: one with full pyrolyzed cells (LIBs), including the casing and another with black mass (BM) from the same batch, which was mechanically processed to remove most metallic fractions (casing and metal foils). It is essential to

note that recycling systems are not perfect; therefore, the BM still contains traces of metallic fractions. On the other hand, LIBs come with the PCB (Printed Circuit Board) plates still attached to the batteries. This distinction is crucial for understanding the differences between laboratory tests and pilot tests, which more closely resemble industrial processes, and the challenges associated with treating complex materials whose average composition is known but whose exact composition is unknown.

For the chemical analysis of LIBs, they were shredded and subsequently was sieved (Retsch Vibratory Sieve Shaker AS 200) into three fractions: a fraction below 125 µm (mainly BM—34.9 mass%), a fraction between 1 mm and 125 µm (30.1 mass%) containing a mixture of BM and metals, and a fraction above 1 mm (mainly metals—35 mass%). Representative samples were generated using a Retsch PT 100 sample divider. Regarding BM, the material already has a fine, granular morphology; therefore, it was analyzed as is. For the product obtained after treatment, the metal shavings generated by drilling holes in the metal block were utilized for chemical analysis. Precipitates from sampling the scrubber solution, before, during and after the experiments were filtered, dried at 100 °C and then the collected powder was analyzed. Slag samples were collected in the molten state throughout the process, including casting. Samples were first crushed below 2 mm (Retsch labor jaw crusher BB51) and then comminuted (Fritsch mono mill "pulverizette 6" or Retsch vibrating mill MM 400) below 65 µm.

Metal and slag samples were dissolved using a microwave digestion method (Anton-Paar—Microwave Reaction System Multiwave PRO) for approximately 1 h, with temperatures ranging between 190 and 210 °C. The digestion process utilized a combination of hydrochloric acid, nitric acid and tetrafluoroboric acid (HBF_4).

For larger metal samples, an open digestion method was employed, involving a heating plate and a Teflon beaker. In this method, aqua regia (a mixture of hydrochloric and nitric acids) and tetrafluoroboric acid were used. Owing to the high sample weight, a large volume of acid was required to ensure complete dissolution. The digestion was brought to a final volume of 1000 mL to minimize the risk of precipitation.

Table 1 presents the average chemical composition of the analyzed LIB and BM samples used during pyrometallurgical treatment, as determined using a "Spectro CIROS Vision" inductively coupled plasma-optical emission spectrometer (ICP-OES) manufactured by SPECTRO Analytical Instruments GmbH, Kleve, Germany. All ICP-OES measurements were performed twice. The carbon and sulphur content was determined using an "ELTRA CS 2000" system made by ELTRA GmbH, Haan, Germany, based on combustion analysis. Fluor was analyzed using a Metrohm ion chromatography IC 881 Compact IC Pro.

For the treatment, a mid-sized Top Blown Rotary Converter (TBRC) of 300 L (100 L working volume) was utilized; details regarding furnace design, reactor configuration and dimensions are presented in Fig. 4a, b. The furnace operates using natural gas, oxygen and air. The refractory material in contact with the slag has a thickness of 160 mm and, according to the supplier (RHI Magnesita Didurit), is composed of a mixture of 87% Al_2O_3, 2% CaO and 8% Cr_2O_3, plus other minor elements. For this experiment, furnace power was adjusted to maintain temperatures between 1450 and 1550 °C, which are ideal for keeping both the produced metal and slag in a liquid state.

During the test, the natural gas consumption was measured precisely. Information provided by the natural gas supplier (Stawag) on the test date was used to calculate the burner's energy consumption. In addition, the ideal amounts of carbon dioxide and carbon generated in ideal combustion were approximated, based on the composition of the natural gas (see Table 2). These values were used to estimate gas generation during the tests, with data from gas analysis and gas flow (measured in L/min) as the basis. Given the high graphite content in both batteries and BM, it was decided to operate with a slightly stoichiometric oxygen excess ($\lambda = 1.05$). Unlike laboratory experiments, in which new crucibles are typically used for each test, pilot- or industrial-scale furnaces may process different materials and slags. Thus, refractories can become contaminated with other metals or mineral slags.

The vessel utilized in the trials had been previously used multiple times for other experiments primarily involving fayalitic slags; therefore, a first test with LIBs was carried out to clean the furnace from the previous tests so that the slag and metal that could remain attached to the vessel are of the same nature as those of the following test presented in this work. This first test also identifies the optimal strategies for charging and handling battery materials.

Table 1 Chemical composition of EoL pyrolyzed NMC LIBs cells and black mass (BM) in wt%

Material	Al	Cu	Mn	Fe	Ni	C	Li	Co	F	Cr	S
Black mass	4.6	2.5	9.5	2.7	14.2	26.8	4.2	10.8	2.3	0.5	0.1
LIB cells	5.8	9.3	12.3	19.9	10.3	21.4	2.8	3.7	1.1	0.4	0.1
−F < 125 µm	0.1	0.9	13.3	1.3	9.9	51.0	3.2	4.0	2.5	0.0	0.1
−125 µm ≤ F < 1 mm	1.6	3.1	24.4	2.7	17.8	10.3	5.4	7.3	0.4	0.0	0.1
−F > 1 mm	15.1	22.9	0.9	53.1	4.2	1.6	0.1	0.2	0.1	1.2	0.0

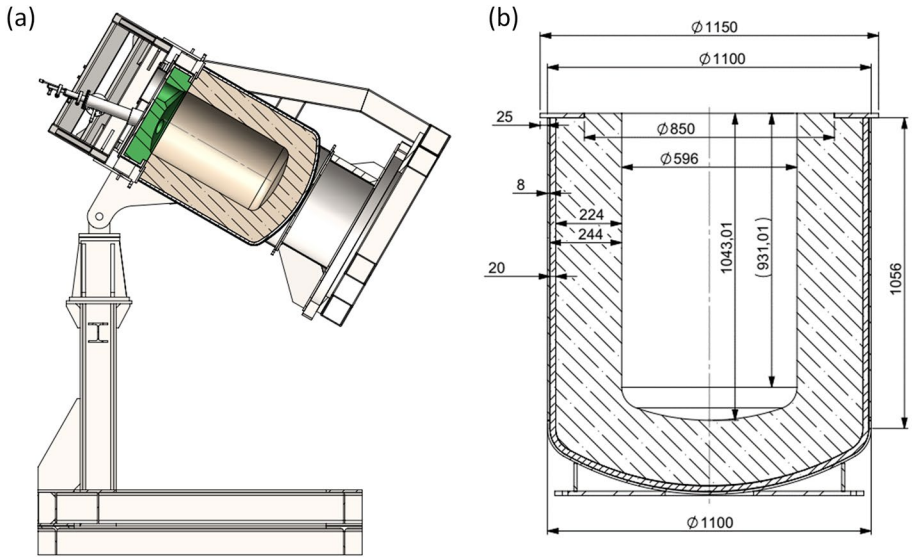

Fig. 4 Mid-size top blown rotary converter at IME RWTH Aachen University: **a** lateral view and **b** vessel dimensions

Table 2 Gas composition and calorific value of the natural gas used during the tests in TBRC, and CO_2 and carbon equivalents (kg/m^3) in SPT

Gas specie	Vol%	Mass%	$CO_2^{eq.}$ (kg/m^3)	$Carbon^{eq.}$ (kg/m^3)
CO_2	1.8%	4.3%	0.032	0.009
N_2	2.9%	4.5%	0.000	0.000
CH_4	88.1%	77.5%	1.585	0.432
C_2H_6	5.5%	9.0%	0.196	0.054
C_3H_8	1.3%	3.1%	0.068	0.019
C_4H_{10}	0.4%	1.2%	0.026	0.007
C_5H_{12}	0.1%	0.3%	0.008	0.002
C_{6+}	0.0%	0.2%	0.004	0.001
Calorific value	11.47 kWh/m^3	1.919 kg/m^3	0.523	

Source Regionnetz, Stawag Aachen, Germany

For the two trials with full cells (the first one to clean the furnace), 186.4 kg of end-of-life (EoL) pyrolyzed lithium batteries from the NMC family were employed alongside additional materials necessary for slag formation: 14.5 kg quartz (Quarzwerke GmbH), 21.75 kg calcined lime (Weissfeinkalk CL90), 26.25 kg calcined Al_2O_3 from Almatis GmbH, and 18.75 kg copper(II) oxide sourced from Lomberg GmbH with Cu_2O content exceeding 98.9 mass%.

Regarding BM treatment, 128 kg were utilized along with 11 kg quartz, 17 kg lime, 35 kg Al_2O_3 and 8 kg Cu_2O to reduce graphite content while lowering melting points within metallic phases; increased amounts of Al_2O_3 were added compared with battery treatments since aluminum foils from the electrodes had been nearly completely removed mechanically.

Initially intended as an automated feeding system for introducing material into the TBRC, the system failed when PCB plates blocked the equipment, necessitating manual loading. BM was placed in textile bags weighing approximately 2 kg each, which were then manually loaded into the furnace.

Before loading material into the TBRC, it is preheated slowly over 1 day until reaching the target process temperatures; in industrial settings, furnaces are never allowed to cool down completely—materials removed after processing are immediately replaced upon reloading—a critical step since rapid heating can damage refractories or cause moisture-induced steam expansion leading to vessel destruction if left unused too long. Table 3 presents the agenda for various steps and trials involving different materials, as well as the EnAM strategies employed to control crystallization.

Temperatures on the furnace lid, the vessel exterior shell and the bottom are monitored continuously. Additionally, the furnace's tilt angle and rotation speed are measured by sensors.

As illustrated in Fig. 5, the exhaust system combines bag filters, cyclones and scrubbers utilizing NaOH solution automatically regulated around pH levels near 10; installations also include flow monitors alongside particle

Table 3 Summary of trial agenda

Trial type	Timing	Description
1st day—Preheating TBRC	10:00 to 23:59—Preheating	Low heating to remove moisture and prevent damage in the refractories
2nd day—Cleaning furnace with LIB material	00:00 to 12:12—Preheating 12:12 to 20:08—Charging 20:08 to 20:08—Holding 21:08 to 21:34—Casting in Ladle 21:34 to 23:59—Preheating	Increase heating until reaching process temperature > 1450 °C Clean the furnace from previous trials utilizing LIBs and fluxes Learning about the charging strategy and handling Casting into a cast-iron ladle (material is discarded)
3rd day—Treating BM	00:00 to 10:20—Preheating 10:20 to 16:56—Charging 16:56 to 17:43—Holding 17:43 to 18:23—Casting in Ladle 18:23 to 23:59—Preheating	Stabilize process temperature > 1450 °C Feeding BM slowly together with fluxes until reaching a homogeneous melt Holding the process until the temperature stabilizes and the graphite from the material is completely combusted Casting into a cast-iron ladle (part of the material will be remelted)
4th to 7th day—Treating LIBs + EnAM	00:00 to 10:00—Preheating TBRC 9:46 to 16:51—Preheating the second controlled temperature furnace 10:00 to 15:50—Charging 15:50 to 16:25—Holding 16:25 to 16:51—Casting into a second furnace 16:51 + 55 h—Control crystallization 7th day—Removing the crucible from the control-unit furnace	Stabilize process temperature in TBRC > 1450 °C Preheat the temperature-controlled unit to 1350 °C Feeding LIBs slowly together with fluxes until reaching a homogeneous melt Holding the process until the temperature stabilizes and the graphite from the material is completely combusted Casting into a second temperature-controlled unit and then cooling at 25 °C/h Remove the crucible after reaching room temperature
8th to 11th day—EnAM from BM	08:00 to 10:00—Removing slag and metal from the casting ladle 10:00 to 10:30—Feeding 25 kg slag into a controlled temperature furnace 10:30 to 14:34—Remelting slag 14:34 + 55 h—Control crystallization 11th day—Removing the crucible from the control-unit furnace	Remelting slag from BM in a temperature-controlled unit to 1450 °C at 400 °C/h + 1 h holding time Cooling the slag at 25 °C/h Remove the crucible after reaching room temperature

measurement sensors pre- and post-cyclone operation monitoring gases such as CO_2, CO, H_2O, NO_x, SO_2, NH_3, HCl, PH_3, HF along various organic molecules like CH_4, C_2H_4, C_2H_6, C_2H_2, etc., throughout experimentation the trials.

The furnace control panel also monitors combustion gas utilization and consumption, rotation, ventilation power and vessel temperature at several points along the ventilation system, providing a comprehensive overview of the process. The exhaust system consists of a sequence of treatments, beginning with air quenching. This is followed by particle separation utilizing a combination of a cyclone and a bag filter. The final stage involves wet separation accomplished by a gas scrubber. To assess the efficiency of the separation stages, particle concentrations are measured before and after the cyclone using two dust-measuring devices (Dusthunter SP100, Sick AG).

In addition to monitoring the fill level, the pH of the scrubber solution is continuously measured using an in-line pH sensor (TB557, ABB Automation Products GmbH). This pH is maintained above 10.5 by the automated addition of highly concentrated sodium hydroxide solutions, dispensed via a metering pump (Delta, ProMinent).

All measurements and control signals are gathered and monitored within a Supervisory Control and Data Acquisition (SCADA) system. The resultant process data are stored in a SQL database and can subsequently be exported for detailed analysis. Following pyrometallurgical treatment, two control cooling approaches were evaluated as the EnAM strategy. For the trial with fully pyrolyzed LIB cells, the material was transferred directly after treatment

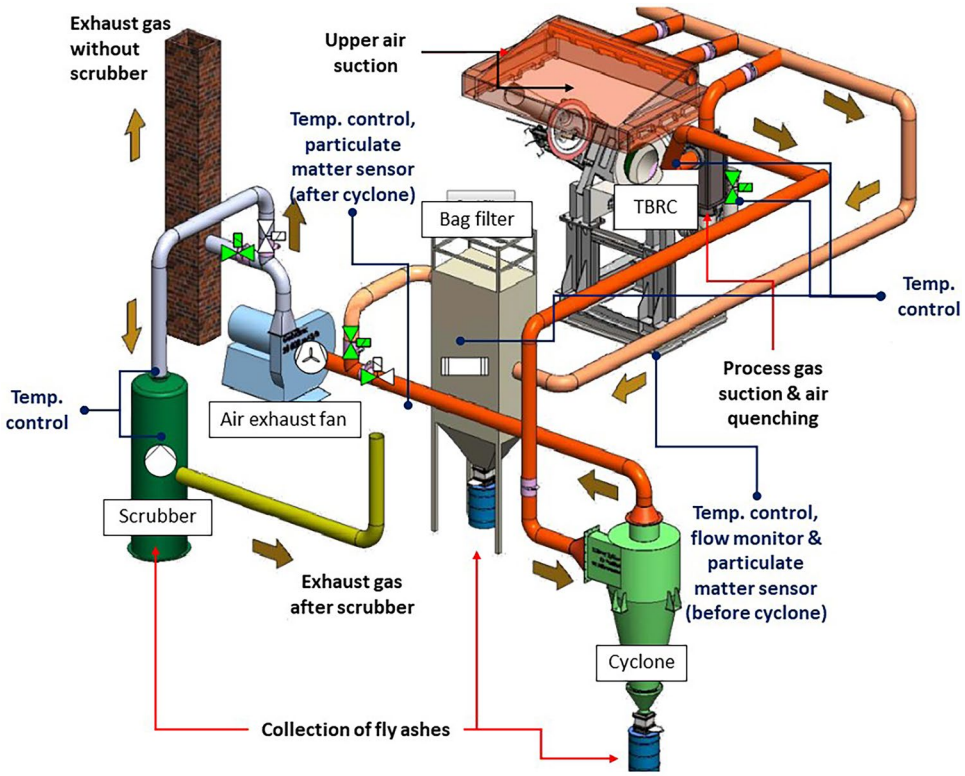

Fig. 5 Exhaust system configuration for the pilot-scale furnaces at IME RWTH Aachen University

into a second temperature-controlled electric furnace (IME-Doppelofen Thermo-Star GmbH) preheated to 1350 °C, then cooled at 25 °C/h until it reached 300 °C (see Fig. 6b, d). This furnace contained a clay-graphite Mars-Isomelt KK600 crucible (ø400/320 mm, *H* 900 mm, volume 68 L, mass ~ 120 kg) manufactured by Gundlach KG.

In contrast, BM allowed ambient air cooling via a cast-iron ladle (Fig. 6a), removing approximately 25 kg (Fig. 6a). This was subsequently placed in a smaller clay–graphite crucible (ø365/285 mm, *H* 600 mm, volume 32 L, mass ~47 kg) made of the same material as the larger one. The material was heated at 400 °C/h to 1450 °C, held for 1 h to ensure a fully liquid state, and then cooled at 25 °C/h using an electric resistance furnace (see Fig. 6d), manufactured by Thermo-Star GmbH. This variation also aims to identify the impact of specific crucible usage when reheating, thereby achieving controlled cooling rates.

According to the manufacturer's data (Gundlach KG), the crucibles used for crystallization have an average composition of graphite (38–46%), SiC + Si (18–28%), Al_2O_3 (10–17%) and SiO_2 (20–26%). Notably, large ceramic crucibles are susceptible to dissolution when in contact with a rich lithium-containing slag, hence the preference for graphite variants.

Products generated during the experiments were analyzed using the same techniques applied earlier to battery materials.

For mineral analysis, the slag samples were analyzed by x-ray diffraction (XRD). In the case of BM, the slag was characterized using an Empyrean diffractometer (Malvern Panalytical, Netherlands). BM slags samples were wet milled using a McCrone mill (Retsch) and prepared in a 27 mm diameter sample holders and the measurement is carried out at 35 kV and 35 mA (Co Kα radiation with Fe-filter) in the 2θ range of 5°–80° while keeping the irradiated area constant (12×15 mm^2) by means of an automated divergence slit. For the quantitative phase determination, Rietveld analysis using the open-source software package Profex/BGMN (suite 5.2.9) [32], with the included crystal structure database (rutile, fluorite, graphite) and additional crystal structures from Tscherry and Schulz (1970) (β-eucryptite), Wong et al. (1987) (γ-$LiAlO_2$), Gummow et al. (2012) (Li_2MnSiO_4), Merlini et al. (2008) (gehlenite), Lucchesi et al. (1994) ($MnAl_2O_4$) and Saburi et al. (1977) (cuspidine), was utilized [33–38]. The amorphous content was determined by adding 20 mass% rutile (TiO_2) as an internal standard. In addition to XRD, images of the samples were acquired using an XL30 environmental scanning electron microscope (ESEM-FEG; FEI Europe B.V., Eindhoven, The Netherlands) with backscattered electron (BSE) imaging.

LIBs slag samples were examined using a PANalytical X'PertPro MP diffractometer in reflection geometry with Co K_α radiation (40 kV and 40 mA), a variable divergence

slit (20 mm irradiated length), primary and secondary soller slits (0.04 rad), anti-scatter slits, a fixed incident beam mask (10 mm), a diffracted beam monochromator and a point detector at BGR. A homogenized portion of the sample was used for the analysis, which was separated using a ripple splitter after mechanical processing of the slag at TU Braunschweig. The finely ground sample was transferred into the sample holder using the backloading preparation method. The measurement was performed in an angular range of 5° to 80° (2θ), with a step size of 0.03° (2θ) and a measurement time of 15 s/step. The amorphous content was determined by adding 20 mass% rutile (TiO_2) as an internal standard. Rietveld refinement was performed using the Profex/BGMN software (suite 5.2.9), with the included crystal structure database (rutile, fluorite, graphite) and additional crystal structures from Pillars & Peacor (1973) (β-eucryptite), Marezio (1965) (γ-$LiAlO_2$), Politaev et al. (2007) (Li_2MnSiO_4), Swainson et al.(1992) (gehlenite), Li et al. (2024) ($Li_xMn_{1-2x}Al_{2+x}O_4$) and Saburi et al. (1977) (cuspidine) [31, 32, 35, 39–42].

To visualize the target phase of the EnAM strategy, γ-$LiAlO_2$, slag blocks have been cut and irradiated with a short-wave UV light (254 nm) source (Raytector (R5-FLS), Raytech Industries (CT, USA).

FactSage 8.4 was used with the FactPS, FToxid and GTOx databases to compare XRD results with predictions generated by FactSage. Using EnAM LIB and BM chemical compositions as references, partial pressures of 1×10^{-10} bar and 1×10^{-12} bar, and temperatures of 500 °C and 1000 °C, were selected. The selected partial pressures were used because the actual oxygen molarity in the samples is unknown, and several components, such as Fe and Mn, exhibit variable oxidation states. Experience showed that in several industrial slags, within this range of partial pressures, models are comparable with the experimental data, particularly when carbon is present in the system [43, 44]. The two selected temperatures enable comparison of mineralogy under conditions in which sufficient energy is present in the system (allowing diffusion and phase precipitation) and under conditions in which the entire sample should be in solid state at a low temperature. In most experimental conditions, slags are far from reaching equilibrium, exhibiting a partially or fully amorphous structure, depending on their chemical composition and cooling rate.

Results

Mass and Energy Balance

Before starting any of the trials, the furnace was preheated slowly over 14 h, consuming 745 kWh of natural gas (equivalent to 77 m^3) and oxygen (equivalent to 133 m^3). This step was necessary to ensure that the vessel was free of moisture and sufficiently hot to increase power and initiate a trial with the material. The second day of trial was dedicated to cleaning the vessel of residues from previous trials (see agenda in Table 3), resulting in an additional 1400 kWh consumption.

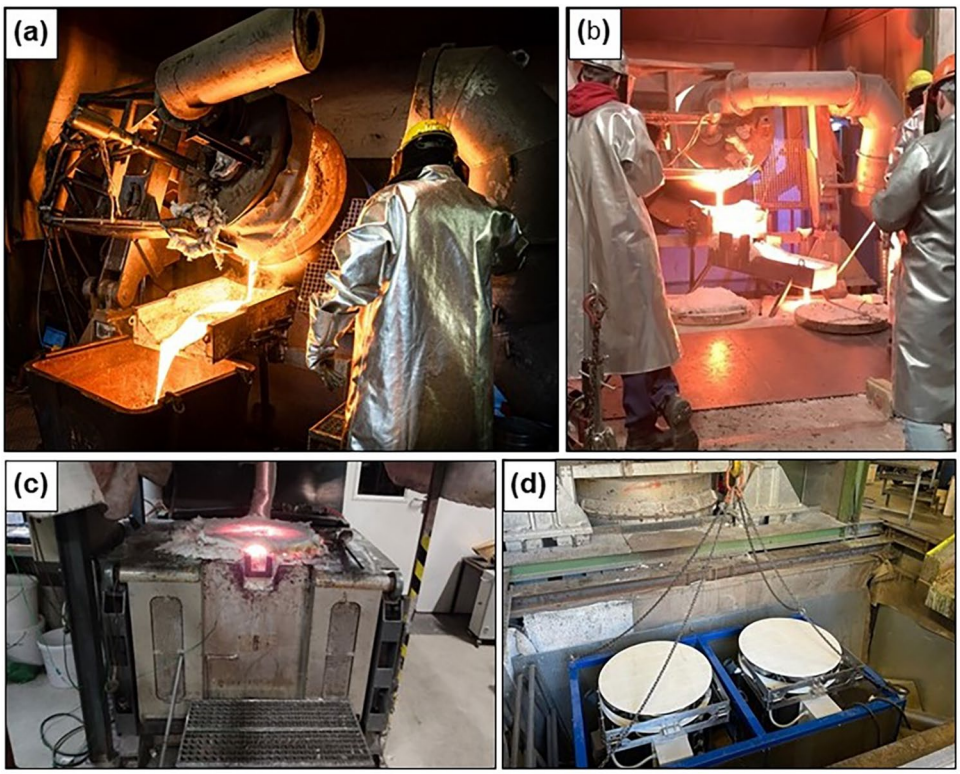

Fig. 6 Furnace utilized for treating LIB material; **a** casting in an iron-ladle, **b** direct casting into a temperature-controlled furnace, **c** furnace for remelting and controlling the cooling of the slag, and **d** furnaces for the direct control of cooling after treatment in TBRC

Table 4 Summary of energy, inputs and outputs during the treatment of black mass in TBRC

Processing		Inputs		Outputs	
Total	1087 kWh	Nat. gas	60.8 m^3	Bag filter	1.0 kg
Burner	61.8%	Oxygen	124.8 m^3	Cyclone	0.1 kg
Rotation	0.4%	Electricity	310.3 kWh	Slag	102 kg
Ventilation	28.1%	Fluxes	71.7 kg	Metal	38 kg
Scrubber	9.6%	BM	128.5 kg	Scrubber[a]	1.9 kg

[a]Taking into account particles and flow sensors after the cyclone

pipeline after the cyclone (4 kg of flue dust, considering the bag filter and cyclone) and should remain in the scrubber. Considering the slag's chemical composition (Table 5), the reduction efficiencies (metal) were 99% for Cu, Ni and Co, 82% for Fe and 45% for Mn. Regarding the slag, it is estimated that 31% of lithium and 74% of fluorine were fumed during the process and ended up as fly ash collected between the cyclone, bag filter and scrubber (with some lithium remaining in solution). Table 7 shows the mass distribution of lithium before and after the pyrometallurgical treatment.

Table 5 Chemical composition of the metal phase in mass% generated during the treatment of black mass in TBRC

Co	Cr	Cu	Fe	Li	Mn	Ni	Si	Sn	C
26.9 ± 0.2	0.9	23.8 ± 0.4	8.3 ± 0.3	< 0.01	5.2 ± 0.3	34.4 ± 0.2	< 0.01	0.36	0.1

Table 6 Chemical composition of slag phase and fly ashes (bag filter and cyclone) in mass% during the treatment of black mass in TBRC

Samples	Cu	Ni	Mn	Ca	Si	Li	Al	Cr	Co	Fe	Na	C	S	F
Bag filter	4.4	1.0	0.7	3.3	1.2	0.5	1.7	0.3	0.4	3.7	0.9	5.4	0.4	14.7
Cyclone	1.2	0.7	0.6	4.7	0.7	0.2	3.9	0.3	0.3	4.0	0.4	2.3	0.8	8,3
Slag	0.1	0.1	6.6	10.1	5.8	3.7	26.5	0.7	0.1	0.3	0.1	0.1	0.0	0.8

Table 7 Estimated mass distribution of lithium throughout the treatment of black mass

Input	Slag	Metal	Bag filter	Cyclone	Solution	Precipitation	Lost in TBRC
5.39 kg	3.74 kg	3.58 g	4.95 g	0.21 g	10.04 g	1.07 kg	0.56 kg

This was performed using the same number of batteries and fluxes as in the trial presented here, with the exception that the material was discarded after the trial. In contrast, this trial maintained the furnace at a high temperature until the next day, when the process presented in this work began consuming a combustion energy equivalent to 848 kWh.

For BM, 200 kg of material, including additives, was loaded. Between loading and processing, 6.9 h were required, consuming 5.4 kWh/kg of feeding material (8.5 kWh/kg BM), with 62% provided by a burner running on natural gas and oxygen. The remaining energy needed was consumed by side equipment (furnace rotation, scrubber pumps and exhaust system). These data have been summarized in Table 4.

After tapping the material into a casting ladle (Fig. 6a), around 38 kg of metal and 102 kg of slag were recovered. Table 5 presents the chemical composition of the metal phase, and Table 6 displays the composition of the material collected in the bag filter, cyclone and slag. It is estimated that approximately 21 kg (15%) may have remained in a residual form inside the furnace. According to the particle sensor, which combines information with the flow, approximately 1.9 kg of material moves through the exhaust system

An initial trial was carried out to treat full LIB cells, which were used not only to clean the furnace but also to learn how to manage the process. Among the first lessons learned was that the feeding system would jam because many of the pyrolyzed batteries are still electrically connected in blocks with a PCB board on top, which wasted extra time and energy. In the second trial with LIBs, the material was manually loaded, which accelerated the trial and resulted in approximately 3.7 kWh/kg of material (5.3 kWh/kg LIBs) consumed in the furnace. The furnace produces nearly the same amount of slag as the BM, which was one of the comparison's goals. Table 8 summarizes the energy and mass balance of the process using full battery cells.

Table 9 presents the composition of the metallic phase obtained from treating the batteries. If we compare the iron content with that obtained from treating BM (Table 5), we can see a threefold increase in concentration. This is because the casing of the treated batteries is made of steel. An increase in iron raises the melting temperature of the metal produced; therefore, it was necessary to increase the

amount of copper oxide to ensure a liquid metallic phase at the test temperature (1500 °C).

Table 10 shows the slag composition and the products collected in the filter, cyclone and scrubber. It is important to note here that the composition of the two slags produced has approximately the same amount of lithium and a fairly similar mineral matrix. The big difference between the slags produced with BM and LIBs is in the manganese content. Treatment with full LIB cells appeared to confer advantages during the process. Because the carbon from the batteries is located within the pyrolyzed cells, the metallic jacket allows the batteries to sink into the slag, thereby releasing their contents. In contrast, BM floats in the slag, increasing the risk that it will be transported more easily by the suction system. This applies not only to carbon but also to fluorine, with the slag from LIB treatment containing almost twice as much fluorine as that from BM.

Manganese oxygen affinity is superior to that of Fe, Co, Ni and Cu. Thermochemical and ideal carbothermic reduction require temperatures above 1450 °C to reduce this element. However, because Mn can be stabilized in the olivine and spinel phases at high temperatures, the element's activity falls and its reduction into metal becomes more difficult. The presence of metallic aluminum foils in LIB cells enables metallothermal reactions, thereby favoring greater manganese reduction. As shown in Eqs. (1) and (2), both carbothermic and metallothermic reactions could happen at 1500 °C. Nevertheless, the delta Gibbs energy gap for the ideal reduction of MnO with Al, compared with C, is seven times larger:

$$\mathrm{MnO} + \mathrm{C} \rightarrow \mathrm{Mn} + \mathrm{CO} \quad \Delta G = -16\ \mathrm{kJ}, \tag{1}$$

$$\mathrm{MnO} + \frac{2}{3}\mathrm{Al} \rightarrow \mathrm{Mn} + \frac{1}{3}\mathrm{Al_2O_3} \quad \Delta G = -118\ \mathrm{kJ}. \tag{2}$$

This difference in Gibbs energy explains why only 45% of manganese was reduced in BM, compared with 83% in the LIB cell treatment. For the remaining metals, the reduction efficiency exceeded 99% for Cu, Co and Ni. In both treatments, between 69 and 77% of the lithium remained immobilized in the slag (the rest was flared). In the case of fluorine, 74% evaporated during BM treatment, compared with only 27% for LIBs.

In both BM and LIB cells, between 70 and 80% of the lithium is immobilized in the mineral phase. The remaining lithium will evaporate as LiF or Li_2O powder. These fly ashes will precipitate throughout the exhaust system, starting with the cyclone, the bag filter and finally the scrubber. Both Table 11 (BM) and Table 12 (LIBs) show that some of the lithium will end up in the alkaline solution of the scrubber (pH 10.5–11.5), while most of the evaporated lithium will precipitate in the sludge (see precipitates in Tables 7, 13).

Table 8 Summary of energy, inputs and outputs during the treatment of LIB cells in TBRC

Processing		Inputs		Outputs	
Total	986.3 kWh	Nat. gas	53.2 m^3	Bag filter	0.94 kg
Burner	59.9%	Oxygen	117.68 m^3	Cyclone	1.99 kg
Rotation	0.4%	Electricity	296.31 kWh	Slag	100 kg
Ventilation	29.6%	Fluxes	81.5 kg	Metal[a]	55 kg (+37 kg)
Scrubber	10.1%	LIB cells	186.4 kg	Scrubber[b]	3.1 kg

[a]92 kg of metal, including what remained in the vessel outside the casting into the temperature-controlled furnace

[b]Taking into account the particles and flow sensors after the cyclone

Table 9 Chemical composition of the metal phase in mass% generated during the treatment of LIBs in TBRC

Co	Cr	Cu	Fe	Li	Mn	Ni	Si	Sn	C
5.8 ± 2.0	0.5 ± 0.2	31.4 ± 14.6	29.7 ± 11.0	< 0.01	13.9 ± 0.6	16.9 ± 1.7	0.5 ± 0.1	0.2 ± 0.1	1.2 ± 0.4

Table 10 Chemical composition of slag phase and fly ashes (bag filter and cyclone) in mass% during the treatment of LIBs in TBRC

Samples	Cu	Ni	Mn	Ca	Si	Li	Al	Cr	Co	Fe	Na	C	S	F
Bag filter	5.8	3.4	2.0	2.2	0.7	1.0	1.6	0.2	1.4	1.8	0.5	15.6	0.3	11.3
Cyclone	6.8	7.0	4.3	6.6	0.7	0.7	3.1	0.2	3.4	3.7	1.0	33.8	0.2	2.2
Slag	0.3	0.2	3.8	8.7	4.7	4.0	19.2	0.3	0.1	0.4	0.7	1.5	0.4	1.4

Table 11 Chemical composition of solutions and precipitates taken from the scrubber during the treatment of black mass in TBRC

Samples Solution	Cu mg/L	Ni	Mn	Ca	Si	Li	Al	Mg	Co	Fe	F	Na g/L	S
Before charging	12.4	< 5	< 5	14.2	< 5	6.0	< 5	14.6	< 5	< 5	173	11.9	4.6
Charging	12.6	< 5	< 5	13.7	< 5	6.3	< 5	14.6	< 5	< 5	178	11.9	4.7
Holding + Casting	15.4	< 5	< 5	13.8	< 5	8.1	< 5	14.9	< 5	< 5	226	12.2	4.9
Precipitates (mass%)													
Charging	14.9	8.5	7.0	4.3	0.9	0.8	0.9	0.3	2.6	9.2	0.1	11.9	0.2
Holding + Casting	17.2	9.5	8.1	4.1	1.1	1.1	1.0	0.3	2.8	6.4	0.2	11.9	0.3

Table 12 Chemical composition of solutions and precipitates taken from the scrubber during the treatment of LIBs in TBRC

Samples Solution	Cu mg/L	Ni	Mn	Ca	Si	Li	Al	Mg	Co	Fe	F	Na g/L	S
Before charging	< 5	< 5	< 5	14.8	< 5	12.4	< 5	9.8	< 5	< 5	298	13.0	4.9
Charging	8.1	< 5	< 5	12.5	< 5	12.0	< 5	9.7	< 5	< 5	307	14.1	4.6
Holding + Casting	10.3	< 5	< 5	11.3	< 5	15.9	< 5	14.0	< 5	< 5	359	14.5	4.8
Precipitates (mass%)													
Charging	16.6	8.8	6.2	3.2	1.0	0.7	0.7	0.3	3.6	3.2	0.4	1.4	0.1
Holding + Casting	12.3	9.0	9.1	7.2	1.0	1.0	0.9	0.8	3.3	3.6	0.3	1.4	0.4

Table 13 Estimated mass distribution of lithium throughout the treatment of LIBs cells

Input	Slag	Metal	Bag filter	Cyclone	Solution	Precipitation	Lost in TBRC
5.20 kg	4.00 kg	0.50 g	9.31 g	14.53 g	16.10 g	0.56 kg	0.60 kg

Emissions

Regarding emissions for the trial with BM only during the material processing step, 63.6 m^3 of natural gas and 129.9 m^3 of oxygen were consumed over the 7.4 h necessary for casting the material. Assuming BM contains 26.8% carbon, the process will generate 248 kg of CO_2, or 1.9 kg CO_2^{eq}/kg BM, if combustion is perfect. Processing full cells required 6.4 h; during this time, 53.2 m^3 of natural gas and 117.7 m^3 of oxygen were consumed. If we consider the carbon content in the cells (21.4% C) and the number of cells fed into the furnace, this would ideally generate 248 kg CO_2^{eq} or 1.3 kg CO_2/kg LIBs.

In the process, not all the carbon is combusted efficiently, and thus several other organic molecules are released. Figure 7 summarizes the gas analysis results by integrating all emissions (vol%) during processing, excluding oxygen, nitrogen and water in gaseous form from the calculation. From these two pie charts, it is clear that treating BM produces more CO and HF emissions than full cells do. Additionally, the abundance of complex organic molecules is higher during BM treatment than in full cells.

Table 14 presents the species generated by the gas detection system during the treatment of BM and LIBs. This estimate was derived from the gas flow rate in the ventilation system, the gas temperature at the flow sensor and the measured gas concentrations.

Several variables can affect these measurements, including air quenching and the dilution factor used by the gas measurement equipment. The accumulated values were corrected on the basis of the assumption that the carbon equivalent of the measured species must equal the carbon released into the extraction system (carbon from combustion and battery material minus what remains immobilized in the slag and the metal phase) plus the CO_2 present in the air (400 ppm). These correlation coefficients, which ranged from 0.47 for BM to 0.4 for LIBs, provide a good estimate of total emissions. Here, it is clear that HF emissions are 2.7 times higher. Fluorine will precipitate throughout the ventilation system, mainly in the scrubber. If we compare the values in Tables 6 and 11 (BM) with those in Tables 10 and 12 (LIBs), all fluorine values are consistently higher in BM. The other big difference is CO, where BM produces seven times more than LIBs.

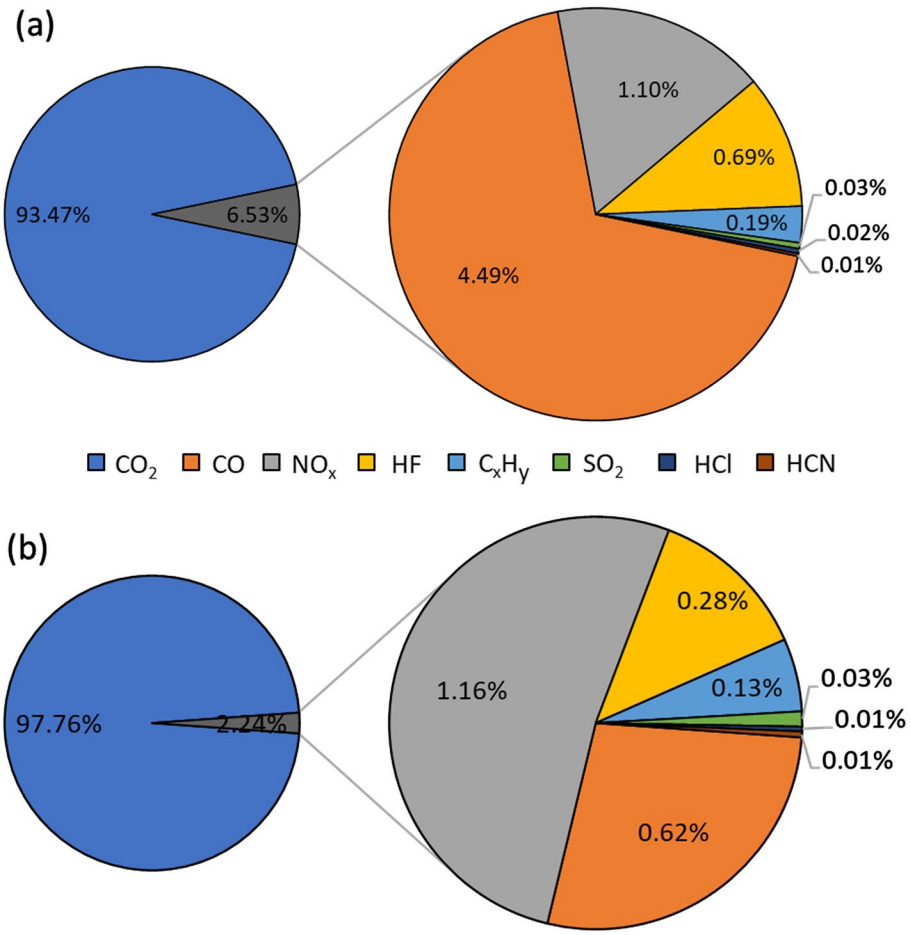

Fig. 7 Volume distribution of gas emission normalized without considering O_2, N_2 and H_2O_{gas} for **a** black mass and **b** full LIB cells

Figure 8 shows the evolution of emissions during the charging, holding and discharging stages. Here, it is clear that most HF emissions occur during charging. It should be noted that HF is an extremely hazardous gas and should be avoided whenever possible. As mentioned in the previous section, the metal capsules of the batteries enable them to enter the slag directly, while the BM floats on the surface. This means that more fluorine is immobilized when the complete cells are processed. Figures 7 and 8 clearly show this phenomenon.

Figure 9 compares the two tests on the same timeline, measured in process hours, using the end of charging (0 h) as the reference point. In this process, it is evident that HF emissions from BM are at least twice those from LIBs.

Although mechanical treatment of batteries enables better recovery of metals from the casing and of Cu and Al foils from the electrodes, pyrometallurgical treatment has proven counterproductive owing to emissions that generate negative environmental impacts. Although fluorine can be immobilized in the scrubber, this does not preclude the possibility that some of these emissions escape the process. In addition, the formation of other fluorine-containing compounds, such as $LiAlF_4$ and Li_2AlF_5 in the gas phase or $LiAlF_4$ and LiF in the slag phase under reducing conditions, could lead to the distribution of fluorine across all three phases (gas, dust and slag), as previously indicated in [12], and evidenced by different fluorine concentrations in both slags (see slag in Tables 6 and 10). Strongly reducing conditions were confirmed by the minimal Cu and Fe contents measured in the slag after metallurgical treatment for both BM and LIBs. In the LIB runs, reduction was further enhanced by metallothermic reactions driven by metallic Al and Fe.

EnAM Strategy

After processing the batteries at 1500 °C, two different cooling strategies were evaluated. Although the slags have different manganese contents, they share quite similar mineral matrices, with approximately 8% Li_2O equivalent. During the LIBs test, they were transferred directly to a second electric furnace (see Fig. 6b), preheated to 1350 °C, and then cooled at 25 °C/h. In the case of BM, it was allowed to cool in the air for several days before being remelted at 1450 °C and cooled at 25 °C/h. This latter strategy has the advantage of not requiring the coupling of two different furnaces, which is technically simpler. On the other hand, remelting

Table 14 Estimated generation of different gas species during the treatment of black mass and full LIB cells in TBRC

Emission	Unit	BM (128.5 kg feed)	LIBs (187.5 kg feed)
CO_2	kg/kg	1.83	1.26
CO	g/kg	49.2	4.70
CH_4 (methane)	g/kg	0.41	0.24
C_2H_6 (ethane)	g/kg	0.10	0.052
C_2H_4 (ethene)	g/kg	0.024	0.038
C_3H_8 (propane)	g/kg	0.084	0.0014
HCHO (formaldehyde)	g/kg	0.0010	0.0011
C_2H_2 (acetylene)	g/kg	0.031	0.012
C_6H_6 (benzene)	g/kg	3.57	0.67
C_7H_8 (toluene)	g/kg	1.43	1.25
NO	g/kg	15.5	10.0
N_2O	g/kg	0.15	0.048
NO_2	g/kg	0.15	0.351
SO_2	g/kg	0.88	0.50
PH_3 (phosphine)	g/kg	0.23	0.041
NH_3	g/kg	0.0047	0.0016
HCl	g/kg	0.40	0.086
HF	g/kg	6.19	1.64
HCN (hydrogen cyanide)	g/kg	0.172	1.25

PH_3, NH_3, HCl, HF, HCN, phenols, organic acids and water-soluble organic compounds are immobilised or neutralized in the scrubber

requires more energy and is conducted at a higher temperature, thereby increasing interaction between the crucible and the slag.

It is essential to note that large crucibles used on an industrial scale are not solely composed of graphite, but rather contain a material comprising graphite and silicon in the form of oxides and carbides. An increase in the residence time of the slag in a liquid state implies greater slag/crucible interaction that will affect the final chemical composition of the obtained material.

If the chemical composition of the slag from the BM treatment in Table 15, obtained at the end of the second remelting (control cooling), is compared with the slag in Table 6. A substantial increase in Al and Si content is evident, undoubtedly attributable to crucible corrosion.

An increase in silica content due to the crucible corrosion leads to an increase in early-crystallizing Li-containing silicates such as Li_2MnSiO_4 (Li_2O~18.6 wt%). An increase in Al leads to the rise of the Li-poor but Al-rich slag phase $Li_xMn_{1-2x}Al_{2+x}O_4$.This phase crystallizes first and extracts a large amount of Al from the melt ($Li_xMn_{1-2x}Al_{2+}xO_4$:Al_2O_3~95 mass%). Consequently, in this melt composition, γ-$LiAlO_2$ competes with $Li_xMn_{1-2x}Al_{2+}xO_4$ for aluminum and with Li_2MnSiO_4 for lithium when it begins to crystallize. This is why the γ-$LiAlO_2$ content is comparatively low (see Table 16). Considering the contamination from the crucible and assuming an ideal composition of γ-$LiAlO_2$, approximately 44% (or 25% when considering the lithium from the input BM) of the lithium available in the BM-EnAM was enriched in the slag as γ-$LiAlO_2$, which could potentially be separated and recovered by flotation [17, 26, 45, 46].

Figure 10 shows BSE images of the slag sample. In addition to large grains of lithium aluminates, the samples exhibit a textural phase with a variable chemical composition around the spinel and gehlenite phases, which could be attributed to the presence of amorphous phases. The results are similar to those of the XRD analysis, with an amorphous fraction of 8%. An interesting aspect of EnAM created by remelting BM slag is that it has a lower percentage of amorphous material compared to full LIB cells (see Table 17), despite having a higher manganese

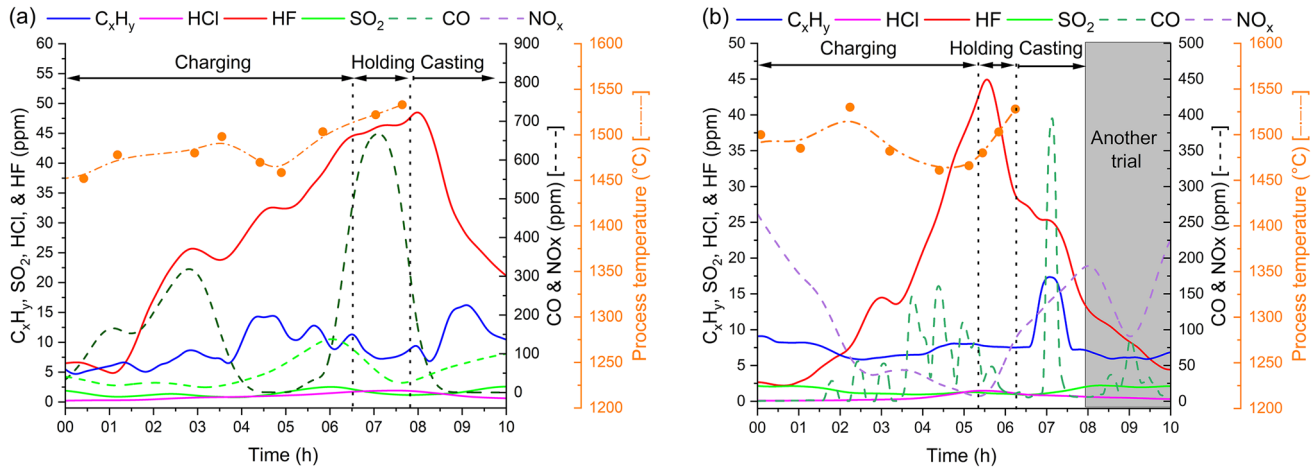

Fig. 8 Emission generated during the treatment of **a** black mass and **b** full LIB cells

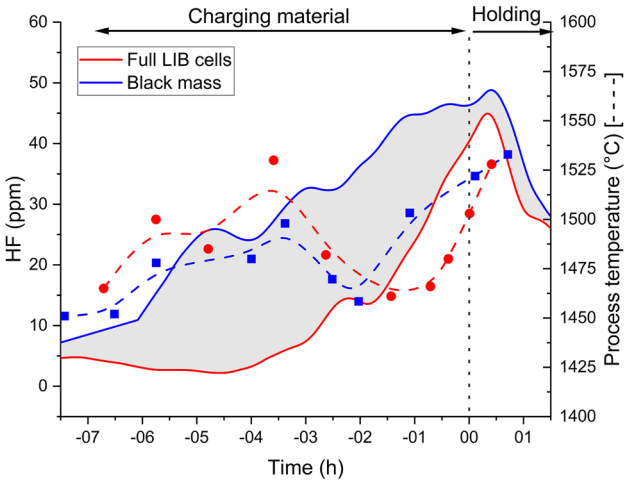

Fig. 9 Comparison of HF emissions between the treatment of black mass and full LIB cells

Figure 11 shows a section of the EnAM created from the BM treatment. γ-$LiAlO_2$ exhibits characteristic green luminescence that distinguishes it from other slag phases, as demonstrated by Marko Ranneberg et al. In this experiment, γ-$LiAlO_2$ forms euhedral crystals with grain sizes of around 1 mm [24, 47].

As shown in Table 17, LIB slag contains twice as much γ-$LiAlO_2$ as BM (see Table 16) and a higher content of amorphous phases. In both slags, the Li content is almost similar (see "Slag" in Tables 6, 10); however, the remelting of BM increases the interaction between the crucible/slag, and the silica content in the slag increases. On the other hand, direct transfer minimizes interaction with crucibles, as solidification begins immediately after transfer, resulting in a substantial increase in γ-$LiAlO_2$ compared with BM treatment. However, it is inevitable that during transfer between furnaces, some of the slag begins to solidify, increasing the amorphous content. Assuming an ideal composition of $LiAlO_2$, approximately 76% of the lithium was enriched in the target phase γ-$LiAlO_2$.

Table 15 Chemical composition of slag phase of black mass produced in TBRC after remelting and cooling at 25 °C/h in TBRC

Cu	Ni	Mn	Ca	Si	Li	Al	Cr	Co	Fe
0.1%	0.1%	5.3%	8.1%	9.4%	3.1%	27.9%	0.4%	0.1%	0.3%

Table 16 Quantitative phase composition based on Rietveld analysis of the slag from the treatment of BM in TBRC in mass%

γ-$LiAlO_2$	β-Eucryptite	Gehlenite	$Li_xMn_{1-2x}Al_{2+x}O_4$	Li_2MnSiO_4	Cuspidine	Fluorite	Amorphous
13	2	30	26	11	6	< 1%	12

Figures of Merit (FoM) of the Rietveld refinement: R_{wp} 8.27%, R_{exp} 4.88%, χ^2 2.87

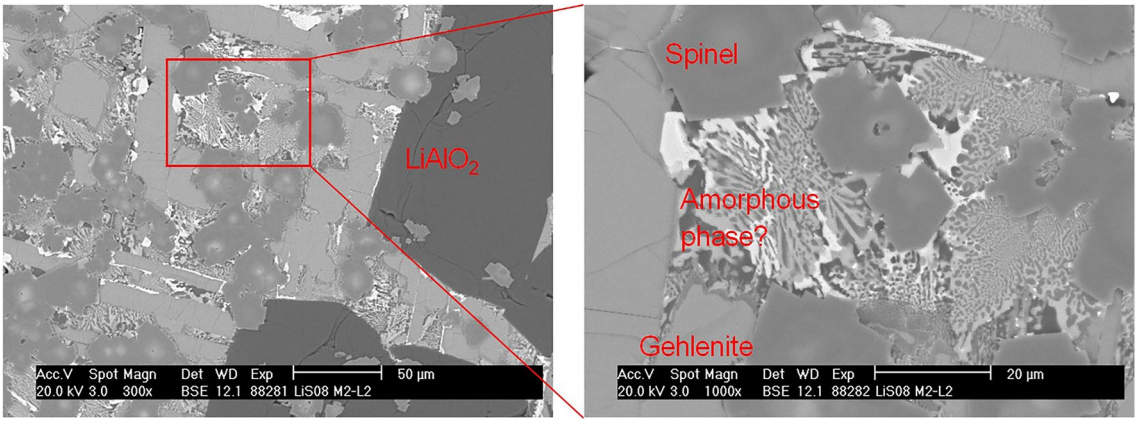

Fig. 10 Scanning electron microscopy (SEM) images of slag from black mass (BM) treatment

concentration in BM. This may be because, in LIBs, a transfer occurred between two furnaces during the same process, potentially producing amorphous material during casting.

Table 17 Quantitative phase composition based on Rietveld analysis of the slag from the treatment of LIBs in TBRC in mass%

γ-$LiAlO_2$	β-Eucryptite	Gehlenite	$Li_xMn_{1-2x}Al_{2+x}O_4$	Li_2MnSiO_4	Cuspidine	Graphite	Fluorite	Amorphous
29	2	11	16	1	8	1	1	31

Figures of Merit (FoM) of the Rietveld refinement: R_{wp} 11.57%, R_{exp} 8.75%, χ^2 1.75

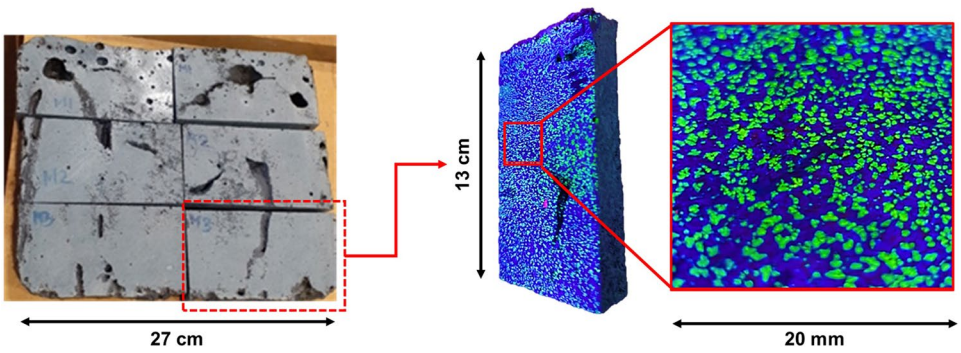

Fig. 11 Li-based EnAM under 254 nm-UV light from black mass treatment in TBRC (γ-$LiAlO_2$ is the green phase)

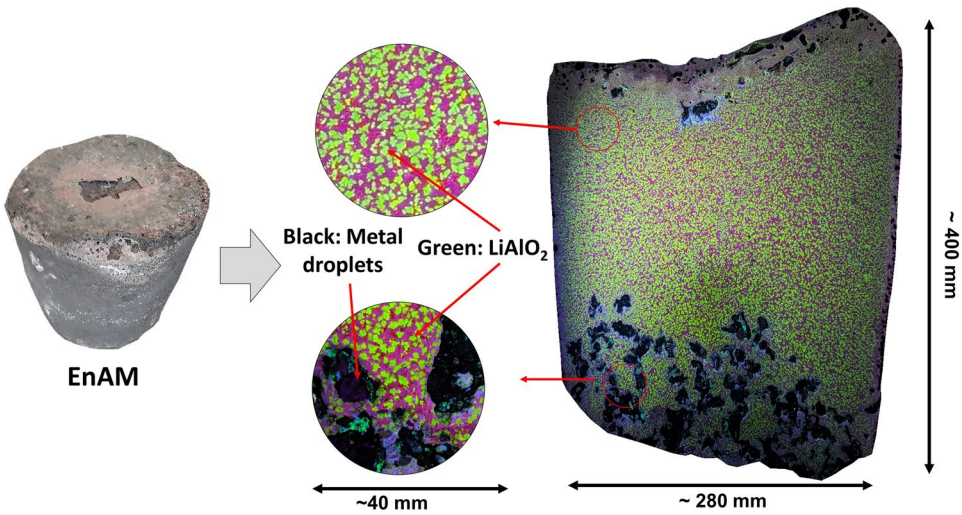

Fig. 12 Li-based EnAM under 254 nm-UV light from full LIB cells treatment in TBRC (γ-$LiAlO_2$ is the green phase) [24]

Figure 12 shows that, under short-wave UV light, the produced block has a higher amount of lithium aluminate grains (green crystals). On the one hand, this demonstrates that it is technically possible to create mineral phases that can be recovered by flotation. At the same time, valuable metals such as Cu, Co and Ni are collected and separated. However, there are also technical aspects that need improvement. Here, the transfer between the two furnaces included the metallic phase, which slowly coagulated at the bottom. As the metal droplets coagulate, they solidify, resulting in numerous metallic inclusions at the bottom of the slag block. Another aspect to consider is that, because crucibles rich in graphite will continue to react with the remaining metal oxides in the slag, gases will become trapped within the mineral structure.

Discussion

Treatment

Figure 13 compares the distribution ratios (L) of selected elements between slag, metal and dust (A) and their overall recoveries (B). Transition metals Cu, Ni and Co exhibit low $L_{slag/metal}$, indicating strong reduction and preferential transfer to the metal. By contrast, Al and Li display high $L_{slag/metal}$, reflecting oxide stability; Li also partly reports to dust in LIBs, consistent with volatility and underscoring the need for off-gas control. Mn and Cr are slag-enriched; in LIBs, Mn shows relatively greater reduction to metal, likely promoted by Fe/Al metallothermy and the

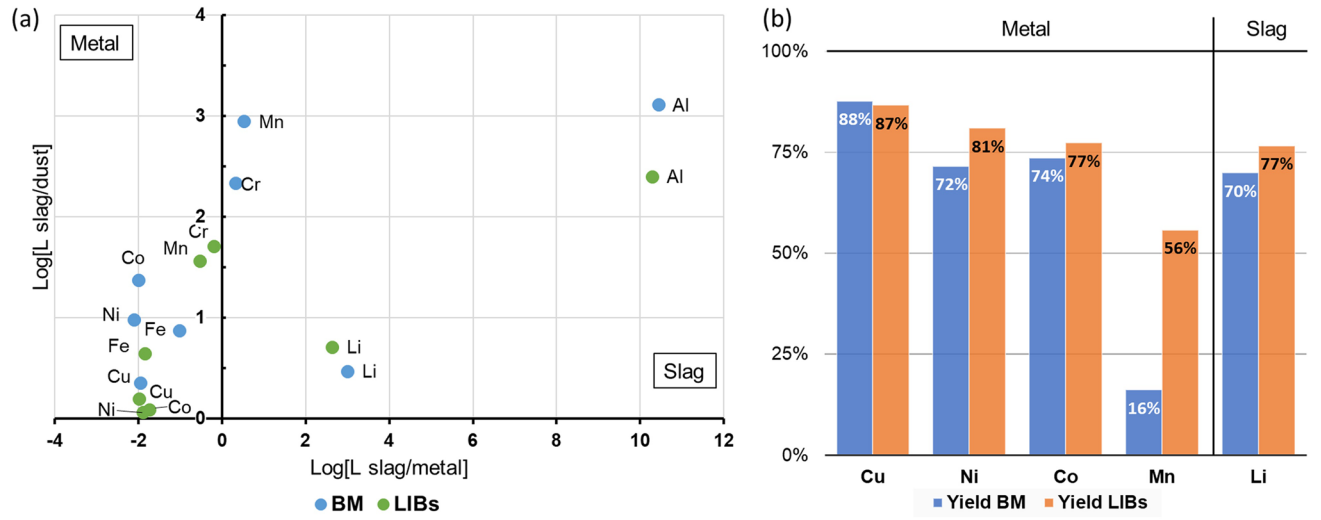

Fig. 13 **a** Element affinity in pyrometallurgical phases (BM versus LIB) and **b** yield of main target elements

stabilization of an Fe-rich alloy. The composition of this LIB alloy should be interpreted cautiously because Cu–Fe immiscibility can bias the measured metal composition.

Normalization to feed mass highlights clear trade-offs between BM and LIB processing. BM treatment concentrates Ni and Co into a Cu–Ni–Co alloy, but it entails a higher specific energy demand and CO_2-equivalent emissions. Fluorine behavior also differs: in BM trials, a larger share volatilizes as HF, whereas in LIBs, more F is immobilized in slag, reducing direct gaseous release but increasing the fluorine inventory that must be managed in the solid phase. LIB smelting is therefore more energy-efficient and less emission-intensive; however, the resulting metallic product has lower direct value because Cu is largely found with Fe.

A critical drawback of LIB processing is that most Cu reports into a coexisting Fe-rich metallic phase. While this alloy stabilizes the system, it complicates downstream refining: producing a Cu-rich product requires a converting stage to oxidize Fe to slag, which also increases the losses of Ni, Co and Mn, thereby increasing energy consumption, flux usage and off-gas generation. In contrast, BM treatment yields a Cu–Ni–Co alloy of higher strategic value.

The yields represented in Fig. 13 indicate consistently higher recoveries for LIBs than for BM across the four targets (Cu, Ni, Li, Co). This can be rationalized by: (i) encapsulation effects—full cells sink and release contents within the bath, limiting dust entrainment compared with floating BM; (ii) stronger metallothermic reduction from Fe and Al in LIB feeds; and (iii) operational/sampling factors for BM (heterogeneity, furnace heel and dust carry-over) that depress measured recoveries. For Li, recoveries remain lower than those of transition metals in both cases, with slightly higher values in LIBs owing to greater immobilization in the slag.

In metallurgical terms, the *L* values reaffirm the robustness of pyrometallurgy for the recovery of transition metals (Cu, Ni, Co) and the segregation of Li, which remains largely in non-metallic phases. BM offers higher product value at the cost of higher energy and gaseous emissions; LIBs provide cleaner operation and higher measured yields, but generate a Cu–Fe alloy that requires further refining. A selective blending strategy could balance these outcomes, leveraging the environmental advantages of LIBs while maintaining alloy value.

EnAM Strategy

The EnAM strategy extends beyond the reuse of slag as a low-cost building material by engineering its composition and controlling crystallization. The goal is to create a stable phase that can be separated and enriched through mechanical methods such as flotation. In the case of rich-bearing Li slags, the formation of $LiAlO_2$ is critical for valorizing the slag phase without compromising the recovery of valuable metals such as Co, Cu, or Ni. In addition to optimizing the slag chemical composition, cooling rates are among the most important parameters. In this regard, reducing cooling rates increases time and energy costs and jeopardizes furnace integrity. In both German projects, DFG-EnAM [19] and the BMFR "greenBatt PyroLith" [48]. This was a subject of extensive internal discussion. Some case cooling rates below 25 °C/h did not achieve full crystallization, especially in slags with high Mn content. Reducing cooling rates also adversely affects the interaction between slags and crucibles. For EnAM samples exceeding 15 kg, there were instances in which the slags fully penetrated the crucibles, thereby destroying the furnace chamber. Higher cooling rates (i.e., 50 °C/h and 100 °C/h) increase the amorphous content,

thereby affecting the formation of $LiAlO_2$. Before the large-scale trials, slags were always remelted and cooled under controlled conditions, as in the case of BM in this study. The transfer of molten slag into a second furnace eliminates the need for remelting, saving time and energy. This was the case of LIB cells. Nevertheless, this process was also associated with an increase in amorphous phases owing to thermal losses during material transfer between furnaces (see amorphous content in Tables 16, 17).

Pilot-scale results demonstrate that, through metallurgical means, it is technically possible not only to recover valuable metals with high efficiency but also to enrich at least 50% of the Li in a phase that can be recovered by flotation. A key aspect of pyrometallurgical treatment is its flexibility in processing various battery families simultaneously. Although part of the lithium is lost in the flue gas (25–30%), another portion remains in slag phases, such as Li_2MnSiO_4 and β-eucryptite, which cannot be easily separated but may require extra steps to valorize this lithium [27]. Once the batteries are processed and slowly cooled—for example, using a thermally insulated ladle—mechanical treatment for grain liberation and flotation would yield a lithium aluminate-containing fraction. The remaining slag becomes enriched in calcium, silicon and manganese oxides with a low Li concentration. These could be returned to the pyrometallurgical process to serve as fluxes for the next batch. The same applies to fly ash; it could also be returned to the process to enhance Li recovery.

One aspect that still needs thorough investigation is the interaction between Li-rich slags and refractory materials. These slags have proven highly corrosive, and refractory manufacturers lack clarity on which refractory material is most suitable for this application. Figure 14 illustrates the evolution of the mineral matrix in the slag, as sampled during the testing of complete cells. It clearly shows a continuous increase in aluminum oxide. Although batteries contain metallic aluminum, they should react quickly during charging in metallothermic reactions. Since part of the refractory material is rich in Al_2O_3, it is believed that this continuous increase is partly owing to corrosion of the refractory material. During furnace unloading and during remelting and controlled cooling, the crucible material also reacted with the slag.

The Challenge of Thermochemical Modelling in Real LIB Slags

During the German Pyrolith project, Li et al. studied in depth the differences between predictions from available thermochemical databases and those from artificial slags produced from mineral matrices derived from battery recycling [31, 49]. Figure 15 compares the mineralogy produced by BM and LIB EnAMs across several models

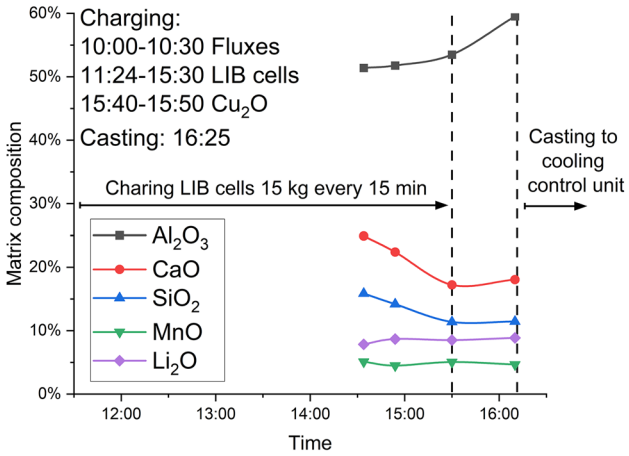

Fig. 14 Evolution of the slag matrix from full LIB cells treatment in TBRC

run at different temperatures and oxygen partial pressures. FToxid and GTOx were used for this comparison. FactSage's FToxid is one of the most powerful databases available for slag modeling. In the two graphs in Fig. 15, it is clear that, under most conditions, and particularly at low temperatures, $LiAlO_2$, which is essential for lithium recovery by flotation, is predicted not to form. This contrasts sharply with the experimental results obtained. The GTOx database was created specifically to evaluate slags for which traditional databases are not suitable. This database accounts for solid lithium and manganese solutions, unlike FToxid. In the LIB models, $LiAlO_2$ is highly optimistic relative to the actual value, which is approximately 29%. For BM, GTOx in many models yields $LiAlO_2$ concentrations that are quite similar to the actual mineralogy. Still, it underpredicts the presence of gehlenite (a member of the Melilite mineral family).

If an overview of the predictions and actual mineralogy is to be given, it can be said that, with the presence of a large amount of amorphous phases, as in the case of LIB cells, FToxid at temperatures and conditions where the slag has not yet reached precipitation ($P_{O_2} = 1 \times 10^{-12}$ bar, $T = 1000$ °C), there is a good prediction of the main mineral phases, except for eucryptite presence. Regarding BM, which, after being completely remelted and cooled, has less amorphous content, GTOx for low temperatures and higher oxygen pressure ($P_{O_2} = 1 \times 10^{-10}$ bar, $T = 500$ °C) predicts the $LiAlO_2$ and spinel phases with almost accurate accuracy.

Because the databases partially predict the phases of the NMC mineral system, they are not suitable for extrapolating when and under which conditions γ-$LiAlO_2$ and β-$LiAlSiO_4$ (both can be separated from the EnAM by flotation [27, 45]) precipitate. GTOx represents an advance over the limitations of FToxid a few years ago, but the predictions still need to be optimized to adequately model Li–Mn-bearing slag systems.

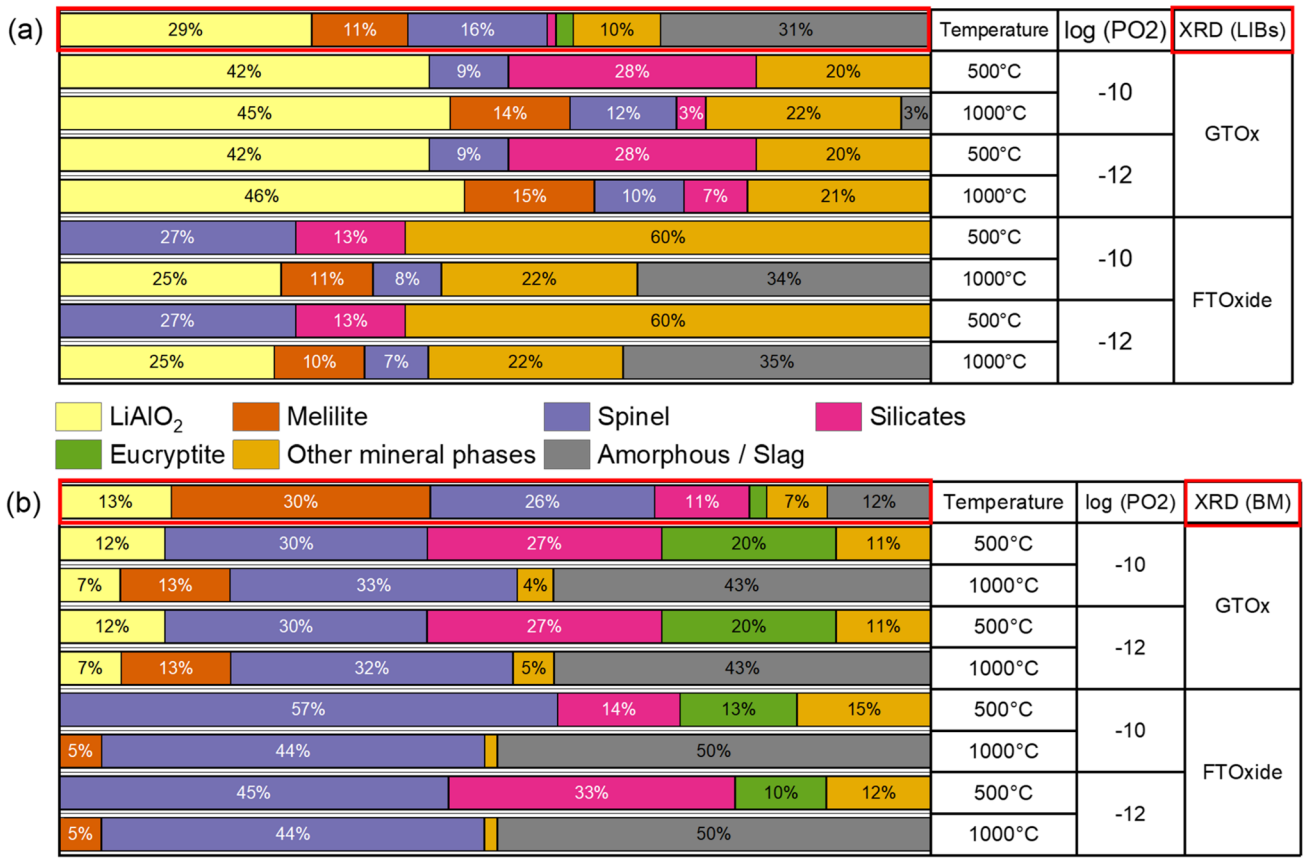

Fig. 15 Comparison between XRD results and thermochemical modeling using GTOx and FToxide FactSage databases, oxygen partial pressures of 1×10^{-10} and 1×10^{-12} bar and temperatures 500 °C and 1000 °C for **a** LiB cells and **b** BM

Potential Exploitation of Experimental Data

In recent years, research on lithium-ion battery recycling has grown exponentially. Most studies have focused on the hydrometallurgical route, mainly at the laboratory scale. However, it is important to note that the metallurgical industry began treating end-of-life (EoL) batteries using a pyrometallurgical stage after simple mechanical disassembly treatments [4, 6, 7].

Life cycle assessment (LCA) and comparisons among different recycling routes are not straightforward. One of the main difficulties lies in the lack of representative data at an industrial scale [50–52]. This is due to several factors:

(i) industrial data is often confidential;
(ii) transparency may be limited for strategic reasons;
(iii) published data mostly come from laboratory tests that do not reflect the actual emissions, energy efficiencies or metallurgical yields of an industrial process.

In particular, laboratory tests are typically conducted on a single battery type or family. In contrast, in industrial practice, a mix of EoL batteries with variable chemistry (NMC, LCO, LFP, etc.) and different technological generations is processed. This heterogeneity introduces significant complexity in the characterization and standardization of the system. It can lead to underestimation of emissions and consumption when laboratory data are extrapolated to industrial scales.

Large-scale tests conducted with real battery mixtures, primarily from the NMC family, though not of the same type, highlight this complexity. In many cases, even pyrolyzed PCBs remain connected to the modules, which increases the difficulty of characterizing the starting battery material and final metallurgical mass balance.

Figure 16 presents a conceptual diagram illustrating how the two tests can be integrated into an industrial recycling process.

In the case of BM, pyrolysis can be performed before or after battery shredding.

Pyrolysis before shredding facilitates subsequent material separation and improves system handling by destroying the electrolyte and reducing operational risks.

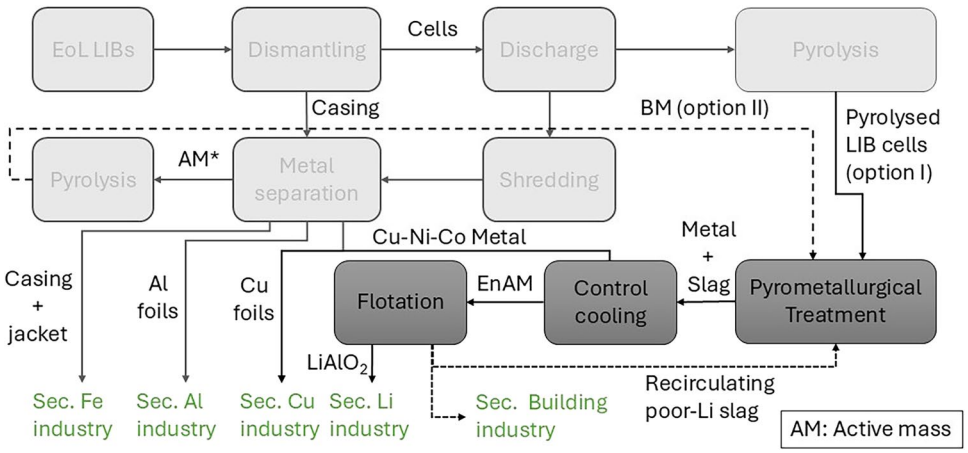

Fig. 16 Lithium battery recycling cycle from a pyrometallurgical perspective. Option I: direct treatment of LIB cells in the furnace; option II: mechanical treatment for metal separation and BM recovery prior to the pyrometallurgical treatment

Pyrolysis after shredding allows for greater homogenization of the material, although it is associated with challenges. However, the presence of manganese, nickel and cobalt oxides in contact with aluminum sheets can promote metallothermic reactions during pyrolysis, thereby reducing aluminum's recyclability.

Furthermore, the separation of the active mass (before pyrolysis) or the BM (after pyrolysis) is never perfect. A fraction of the active material remains attached to the electrical collectors (Al and Cu foils).

In the case of copper, this is not a significant problem, as it is a more noble metal, and the copper industry can recover the accompanying metals. For aluminum, the situation is more critical. The high affinity of Al for oxygen favors the formation of compounds in which nickel, cobalt and copper can become metallurgically trapped in recycled aluminum, thereby complicating their economic separation. This may involve discarding these sheets or necessitating additional cleaning treatments. Direct furnace treatment of cells may be reasonable if the economic value of the aluminum foils is not a priority. This option reduces the number of processing stages, eliminates the need to sort by battery families (LCO, NMC, LFP) and chemistries, and simplifies operational logistics.

The ferrous fraction in various cell types (e.g., casings, jackets) can be preseparated using magnetic separators, thereby improving overall metal recovery.

In the case of BM, pyrolysis can be performed before or after battery shredding.

Pyrolysis before shredding facilitates subsequent material separation and improves system handling by destroying the electrolyte and reducing operational risks.

Pyrolysis after shredding allows for greater homogenization of the material, although it is associated with challenges. However, the presence of manganese, nickel and cobalt oxides in contact with aluminum sheets can promote metallothermic reactions during pyrolysis, thereby reducing aluminum's recyclability.

Pyrometallurgical treatment typically generates:

- metal fraction rich in Cu, Ni, Co and Mn;
- Li–Mn-rich slag;
- flue dust and scrubber liquid solutions and precipitates.

The natural destination of the metal fraction is the copper industry, where refining processes enable efficient separation of Ni, Co and other accompanying metals via intermediate unit operation [53–55].

An aspect often underestimated in LCA is the presence of PCBs in battery modules. These contain Cu, Ag and Au, which—although in low concentrations—can be recovered during copper refining, contributing positively to the environmental and economic balance of the process [56].

The main challenge of pyrometallurgical treatment is the behavior of lithium.

Lithium is primarily distributed in slag, often as γ-$LiAlO_2$ in the EnAM strategy, in fly ash and in scrubber streams (in solution or as fluoride-rich precipitates).

Although the immobilization of Li as $LiAlO_2$ is incomplete, separating this phase yields a mineral mix almost depleted in Li and Al. From a process perspective, this is an advantage because the remaining components are the fluxes utilised in the pyrometallurgical process. The partial presence of Li in slag and fly ash enables recirculation; in consecutive batch processes, this recirculation can enhance Li content in the slag phase and thus enhance Li-bearing mineral phases that could be separated in a subsequent flotation step.

The lithium present in solution in the scrubber could potentially be treated with Na_2CO_3 to produce Li_2CO_3. This aspect requires further research and experimental validation, particularly regarding purity, chemical consumption and economic viability.

Table 18 presents a summary of inputs and outputs of the pyrometallurgical process, normalized to 1 kg of BM or LIB cells.

Table 18 Summary of energy and mass balances normalized by 1 kg of treated LIB material

Inputs	1 kg BM	1 kg LIB cells
Cu_2O	0.06 kg/kg BM	0.10 kg/kg LIBs
Al_2O_3	0.27 kg/kg BM	0.10 kg/kg LIBs
Limestone	0.13 kg/kg BM	0.14 kg/kg LIBs
Quartz	0.09 kg/kg BM	0.08 kg/kg LIBs
Thermal energy (burner)	5.23 kWh/kg BM	3.17 kWh/kg LIBs
–Natural gas	0.47 Nm^3/kg BM	0.29 Nm^3/kg LIBs
–Oxygen	0.97 Nm^3/kg BM	0.62 Nm^3/kg LIBs
Electricity (TBRC engines)	0.03 kWh/kg BM	0.02 kWh/kg LIBs
Electricity (exhaust system)	3.19 kWh/kg BM	2.10 kWh/kg LIBs
Electricity (control cooling)	1.92 kWh/kg BM	1.89 kWh/kg LIBs
Scrubber		
–Water	36.56 dm^3/kg BM	27.07 dm^3/kg LIBs
–NaOH	0.51 g/kg BM	0.34 g/kg LIBs
Products	1 kg BM	1 kg LIB cells
Metal alloy	0.30 kg/kg BM	0.49 kg/kg LIBs
Slag	0.79 kg/kg BM	0.54 kg/kg LIBs
–$LiAlO_2$	0.10 kg/kg BM	0.16 kg/kg LIBs
–Potentially recoverable Li	10.32 g/kg BM	15.56 g/kg LIBs
–Sec. building material or recirculation in furnace	0.69 kg/kg BM	0.38 kg/kg LIBs
Material losses	1 kg BM	1 kg LIB cells
Metal alloy	0.03 kg/kg BM	0.05 kg/kg LIBs
Slag	0.08 kg/kg BM	0.05 kg/kg LIBs
Solid wastes	1 kg BM	1 kg LIB cells
Flue dust	0.02 kg/kg BM	0.03 kg/kg LIBs
Clay–Graphite crucible	0.09 kg/kg BM	0.64 kg/kg LIBs
Liquid emissions	1 kg BM	1 kg LIB cells
Water	35.77 dm^3/kg BM	26.73 dm^3/kg LIBs
–Cu	4.30 mg/kg BM	1.48 mg/kg LIBs
–Ni	< 1.50 mg/kg BM	< 1.00 mg/kg LIBs
–Fe	< 1.50 mg/kg BM	< 1.00 mg/kg LIBs
–Mn	< 1.50 mg/kg BM	< 1.00 mg/kg LIBs
–Co	< 1.50 mg/kg BM	< 1.00 mg/kg LIBs
–Mg	4.16 mg/kg BM	2.01 mg/kg LIBs
–Ca	3.83 mg/kg BM	1.62 mg/kg LIBs
–Li	2.25 mg/kg BM	2.28 mg/kg LIBs
–Na	3.41 mg/kg BM	2.08 mg/kg LIBs
–S	< 1.50 mg/kg BM	< 1.00 mg/kg LIBs
–Cl	8.12 mg/kg BM	4.34 mg/kg LIBs
F	62.79 mg/kg BM	51.49 mg/kg LIBs

Several gas components are neutralized in the scrubber, forming precipitates. Air emissions are shown in Table 14

The aim is for this data to be used by the scientific community to:

- improve the quality of inventories in LCA studies;
- reduce dependence on laboratory data alone,
- enable more realistic comparisons between pyrometallurgical and hydrometallurgical routes.

An online supplementary Excel document is also available, providing detailed information on mass balances, energy consumption and elemental distributions to promote greater transparency and reproducibility in future studies.

Conclusion

This study addressed a gap in Li-ion battery recycling by generating transparent pilot-scale datasets on mass balances, energy consumption and emissions for pyrometallurgical processing in a top-blown rotary converter. Black mass and full NMC cells were treated under comparable conditions, allowing direct assessment of process efficiency, environmental impact and product quality.

Cu, Ni and Co were recovered with near-quantitative efficiency, although the resulting alloys differed in composition. Black mass yielded a Cu–Ni–Co alloy of high strategic value, whereas full-cell treatment produced a Cu–Fe alloy that would require additional refining. Environmental performance also diverged: black mass processing required more energy and emitted more gaseous emissions, whereas full-cell treatment immobilized more fluorine in the slag and had a lower CO_2 intensity. In addition, key challenges were identified, including HF and organic emissions during black mass treatment, refractory corrosion under Li-rich slags and alloy immiscibility during the processing of full LIB cells.

The Engineering of Artificial Minerals (EnAM) strategy was successfully demonstrated, with controlled cooling stabilizing a significant share of Li as γ-$LiAlO_2$ suitable for recovery by flotation. It is often believed that at the end of their life cycle, batteries from the same family with similar technical characteristics will be easily recoverable and separable for use in hydrometallurgical processes optimized for those batteries. The reality is that batteries constantly evolve, and at the end of their life cycle, companies responsible for their recovery will only be able to process batches containing batteries that are similar, but not necessarily identical. Additionally, the presence of electronic components further increases the chemical complexity of these wastes. This is where pyrometallurgy has a significant advantage: its ability to treat complex multi-waste streams in a single process.

Finally, this work shows that pyrometallurgy, while robust for transition-metal recovery, can also be adapted for partial Li valorization through slag engineering. By providing realistic pilot-scale data and highlighting both opportunities and limitations, it establishes a solid foundation for future life-cycle and techno-economic assessments and for advancing industrial implementation.

Supplementary Information The online version of this article (https://doi.org/10.1007/s40831-026-01488-x) contains supplementary material, which is available to authorized users.

Acknowledgements The authors acknowledge the financial support of the German Federal Ministry of Education and Research (BMBF) within the cluster project, "greenBatt PyroLith" (grant no. 03XP0336B) and the German Research Foundation within the Priority Program "Engineered Artificial Minerals (EnAM)—a geo-metallurgical tool to recycle critical elements from waste streams" (grant no. 470552553). Additional support was provided by the BMBF through the DiRectION Project (grant no. 03XP0358C), which contributed technology and expertise in digitalization relevant to the sensor systems used to monitor energy consumption and gas emissions in these experiments.

Funding Open Access funding enabled and organized by Projekt DEAL.

Declarations

Conflict of Interest The authors report no conflicts of interest.

References

1. Sojka R, Pan Q, Billmann L (2020) Comparative study of Li-ion battery recycling processes. ACCUREC Recycling GmbH, Krefeld
2. Wagner-Wenz R, van Zuilichem A-J, Göllner-Völker L et al (2023) Recycling routes of lithium-ion batteries: a critical review of the development status, the process performance, and life-cycle environmental impacts. MRS Energy Sustain 10:1–34. https://doi.org/10.1557/s43581-022-00053-9
3. Salces AM, Bremerstein I, Rudolph M, Vanderbruggen A (2022) Joint recovery of graphite and lithium metal oxides from spent lithium-ion batteries using froth flotation and investigation on process water reuse. Miner Eng 184:107670. https://doi.org/10.1016/j.mineng.2022.107670
4. Klimko J, Oráč D, Miškufová A et al (2020) A combined pyro- and hydrometallurgical approach to recycle pyrolyzed lithium-ion battery black mass Part 2: lithium recovery from Li enriched slag—Thermodynamic study, kinetic study, and dry digestion. Metals 10:1558. https://doi.org/10.3390/met10111558
5. Friedrich B, Lucas H, Stallmeister C (2024) Pyrometallurgical concepts for recovery of lithium, cobalt and nickel from spent batteries. In: SAIMM 2024, 2024
6. Elwert T, Goldmann D, Strauss K, Schirmer T (2012) Phase composition of high lithium slags from the recycling of lithium ion batteries. World Metall Erzmetall 65(3):163–171
7. Georgi-Maschler T, Friedrich B, Weyhe R et al (2012) Development of a recycling process for Li-ion batteries. J Power Sources 207:173–182. https://doi.org/10.1016/j.jpowsour.2012.01.152
8. Scheunis L, Yagi R (2025) Recovery of nickel and cobalt from black mass. WO/2023/217710
9. Yagi R, Scheunis L (2022) Recovery of nickel and cobalt from Li-ion batteries or their waste. WO2022248245A1
10. Yagi R, Scheunis L (2023) Récuperation de nickel et de cobalt à partir de masse noire. WO2023217710A1
11. Scheunis L, Callebaut W (2024) Process for the recovery of lithium. US11952643B2
12. Geimer S, Reuter MA, Borowski NPK, Hecker E (2023) Method for recycling Li-ion batteries. US Patent App. 18/579,340
13. Handayani S, Shahril WI, Ismojo I et al (2024) Mass balance of nickel manganese cobalt cathode battery recycle process. J Bioresour Environ Sci 3:161–165. https://doi.org/10.61435/jbes.2024.19939
14. Sun Y, Yang H, Li J et al (2024) A large volume and low energy consumption recycling strategy for $LiNi_{0.6}Co_{0.2}Mn_{0.2}O_2$ from spent ternary lithium-ion batteries. J Power Sources 602:234407. https://doi.org/10.1016/j.jpowsour.2024.234407
15. Orac D, Vaskova I, Klimko J et al (2024) Overview of recycling techniques for lithium-ion batteries. Kem Ind 73:147–152. https://doi.org/10.15255/KUI.2023.030
16. Brückner L, Frank J, Elwert T (2020) Industrial recycling of lithium-ion batteries—A critical review of metallurgical process routes. Metals 10:1107. https://doi.org/10.3390/met10081107
17. Qiu H, Li H, Fischlschweiger M et al (2024) Valorisation of lithium containing slags from pyrometallurgical recycling route of spent lithium-ion batteries: the enrichment of γ-$LiAlO_2$ phase from thermodynamic controlled and modified slags. Miner Eng 217:108918. https://doi.org/10.1016/j.mineng.2024.108918
18. Davris P, Stopic S, Balomenos E et al (2017) Leaching of rare earth elements from eudialyte concentrate by suppressing silica gel formation. Miner Eng 108:115–122. https://doi.org/10.1016/j.mineng.2016.12.011
19. Priority Programme "Engineered Artificial Minerals (EnAM)—a geo-metallurgical tool to recycle critical elements from waste streams" (SPP 2315). https://www.dfg.de/de/aktuelles/neuigkeiten-themen/info-wissenschaft/2023/info-wissenschaft-23-96. Accessed 13 Feb 2026
20. Qiu H (2023) The development of a process for the recovery of lithium from pretreated slags by means of flotation. PhD Thesis, Clausthal University of Technology
21. Elwert T, Goldmann D, Schirmer SK (2012) Recycling von Li-Ionen Traktionsbatterien – Das Projekt LIBRI, 2012th edn. TK Verlag, Baden-Wurttemberg
22. Peuker P (nd) Kompetenzcluster Recycling & Grüne Batterie (greenBatt). www.greenbatt-Clust
23. Hellmers S, Ranneberg M, Böttcher A-C, Kwade A (2022) Determination of lithium aluminate content in lithium ion batteries' slag using short-wave ultraviolet and picture analysis in liberation. In: International battery production conference, 2022
24. Ranneberg M, Graupner T (2024) Schlussbericht des Teilvorhabens der BGR-Arbeitsgruppe „Mineralphasen- und Strukturanalytik Li-haltiger Schlacken" zum BMBF Verbundprojekt PyroLith. Bundesanstalt für Geowissenschaften und Rohstoffe, Hannover
25. Rannerberg M, Lucas HI, Li H et al (2023) Evaluation of Li and Mn influence on Al–Ca–Si–O slag system regarding pyrometallurgical LIBs treatment. In: 8th International slag valorisation symposium, 2023, Mechelen, Belgium, pp 205–209
26. Ranneberg M, Graupner T, Goldmann S (2022) Chemical and mineralogical characterisation of Li- and Mn-bearing slags to increase the recycling efficiency of lithium from lithium-ion-batteries (LIB). https://doi.org/10.48380/YJ0R-VB37

27. Qiu H, Li H, Fischlschweiger M et al (2025) A study of the floatability and leaching behavior of eucryptite and eucryptite-containing slag. Results Eng 27:105702. https://doi.org/10.1016/j.rineng.2025.105702
28. Lucas H, Stallmeister C, Friedrich B (2024) Schlussbericht des Teilvorhabens der IME-Arbeitsgruppe „Schmelzmetallurgie“ zum BMBF Verbundprojekt PyroLith. RWTH Aachen-IME-“Institut für Metallurgische Prozesstechnik und Metallrecycling,” Hannover
29. Rachmawati C, Weiss J, Lucas HI et al (2024) Characterisation of the grain morphology of artificial minerals (EnAMs) in lithium slags by correlating multi-dimensional 2D and 3D methods. Minerals 14:130. https://doi.org/10.3390/min14020130
30. Wittkowski A, Schirmer T, Qiu H et al (2021) Speciation of manganese in a synthetic recycling slag relevant for lithium recycling from lithium-ion batteries. Metals 11:188. https://doi.org/10.3390/met11020188
31. Li H, Qiu H, Ranneberg M et al (2024) Enhancing lithium recycling efficiency in pyrometallurgical processing through thermodynamic-based optimization and design of spent lithium-ion battery slag compositions. ACS Sustain Resour Manag. https://doi.org/10.1021/acssusresmgt.4c00064
32. Doebelin N, Kleeberg R (2015) *Profex* : a graphical user interface for the Rietveld refinement program *BGMN*. J Appl Crystallogr 48:1573–1580. https://doi.org/10.1107/S1600576715014685
33. Tscherry V, Schulz H (1970) Structure and superstructure of β-eucryptite. Naturwissenschaften 57:194–194. https://doi.org/10.1007/BF00592979
34. Wong-Ng W, McMurdie HF, Paretzkin B et al (1987) Standard X-ray diffraction powder patterns of fifteen ceramic phases. Powder Diffr 2:106–117. https://doi.org/10.1017/S0885715600012495
35. Saburi S, Kawahara A, Henmi C et al (1977) The refinement of the crystal structure of Cuspidine. Mineral J 8:286–298. https://doi.org/10.2465/minerj.8.286
36. Gummow RJ, Sharma N, Peterson VK, He Y (2012) Crystal chemistry of the *Pmnb* polymorph of Li_2MnSiO_4. J Solid State Chem 188:32–37. https://doi.org/10.1016/j.jssc.2012.01.051
37. Merlini M, Gemmi M, Cruciani G, Artioli G (2008) High-temperature behaviour of melilite: in situ X-ray diffraction study of Gehlenite–Åkermanite–Na melilite solid solution. Phys Chem Miner 35:147–155. https://doi.org/10.1007/s00269-007-0206-2
38. Lucchesi S, Della Giusta A (1994) Crystal chemistry of non-stoichiometric Mg–Al synthetic spinels. Z Kristallogr Cryst Mater 209:714–719. https://doi.org/10.1524/zkri.1994.209.9.714
39. Pillars WW, Peacor DR (1973) The crystal structure of beta eucryptite as a function of temperature. Am Mineral 58:681–690
40. Marezio M (1965) The crystal structure and anomalous dispersion of γ-$LiAlO_2$. Acta Crystallogr 19:396–400. https://doi.org/10.1107/S0365110X65003511
41. Politaev VV, Petrenko AA, Nalbandyan VB et al (2007) Crystal structure, phase relations and electrochemical properties of monoclinic Li_2MnSiO_4. J Solid State Chem 180:1045–1050. https://doi.org/10.1016/j.jssc.2007.01.001
42. Swainson IP, Dove MT, Schmahl WW, Putnis A (1992) Neutron powder diffraction study of the akermanite–gehlenite solid solution series. Phys Chem Miner. https://doi.org/10.1007/BF00202107
43. Alkan G, Mechnich P, Lucas H et al (2022) Assessment of metallurgical slags as solar heat absorber particles. Minerals 12:121. https://doi.org/10.3390/min12020121
44. Lucas H, Weiss J, Friedrich B (2024) Modelling pyrometallurgical systems through oxygen partial pressure to fit experimental data: “Study case: fayalitic slags”. In: GTT users’ meeting 2024, 2024
45. Qiu H, Degenhardt C, Feuge N et al (2022) Influencing the froth flotation of $LiAlO_2$ and melilite solid solution with ionic liquids. RSC Adv 12:29562–29568. https://doi.org/10.1039/D2RA02922G
46. Hellmers S, Qiu H, Ranneberg M et al (2024) Lithium recovery from pyrometallurgical slags through dry milling and flotation. In: Advanced battery power, 2024, Munster, Germany
47. Ranneberg M, Graupner T (2023) Development of a routine method for the chemical and mineralogical characterisation of Li- and Mn-containing slags from the recycling of NMC-type lithium-ion batteries (LIBs). In: GeoBerlin, 2023, Berlin
48. Peuker P (nd) PyroLith - greenBatt - Rückgewinnung von Li aus Mn-haltigen Schlacken. www.greenbatt-Clust. https://www.greenbatt-cluster.de/en/projects/pyrolith/. Accessed 13 Feb 2026
49. Li H, Qiu H, Schirmer T et al (2022) Tailoring lithium aluminate phases based on thermodynamics for an increased recycling efficiency of Li-ion batteries. ACS EST Eng 2:1883–1895. https://doi.org/10.1021/acsestengg.2c00105
50. Erakca M, Pinto Bautista S, Moghaddas S et al (2023) Closing gaps in LCA of lithium-ion batteries: LCA of lab-scale cell production with new primary data. J Clean Prod 384:135510. https://doi.org/10.1016/j.jclepro.2022.135510
51. Perocillo YK, Pirard E, Léonard A (2025) Process simulation-based LCA: Li-ion battery recycling case study. Int J Life Cycle Assess 30:2494–2518. https://doi.org/10.1007/s11367-025-02478-z
52. Barbosa JC, Pinto RS, Serra JP et al (2025) Batteries and sustainability: the relevance of life cycle assessment. Sustain Energy Technol Assess 82:104488. https://doi.org/10.1016/j.seta.2025.104488
53. Tran TT, Moon HS, Lee MS (2022) Recovery of cobalt, nickel and copper compounds from UHT processed spent lithium-ion batteries by hydrometallurgical process. Miner Process Extr Metall Rev 43:453–465. https://doi.org/10.1080/08827508.2021.1910508
54. Agrawal A, Manoj MK, Kumari S et al (2008) Extractive separation of copper and nickel from copper bleed stream by solvent extraction route. Miner Eng 21:1126–1130. https://doi.org/10.1016/j.mineng.2008.02.016
55. Davenport WG, King M, Schlesinger M, Biswas AK (2002) Chemical metallurgy of copper recycling. In: Extractive metallurgy of copper. Elsevier, Amsterdam, pp 355–365
56. Pokhrel P, Lin S-L, Tsai C-T (2020) Environmental and economic performance analysis of recycling waste printed circuit boards using life cycle assessment. J Environ Manag 276:111276. https://doi.org/10.1016/j.jenvman.2020.111276